Joule

CellPress

Article

Thermal Runaway of Lithium-Ion Batteries without Internal Short Circuit

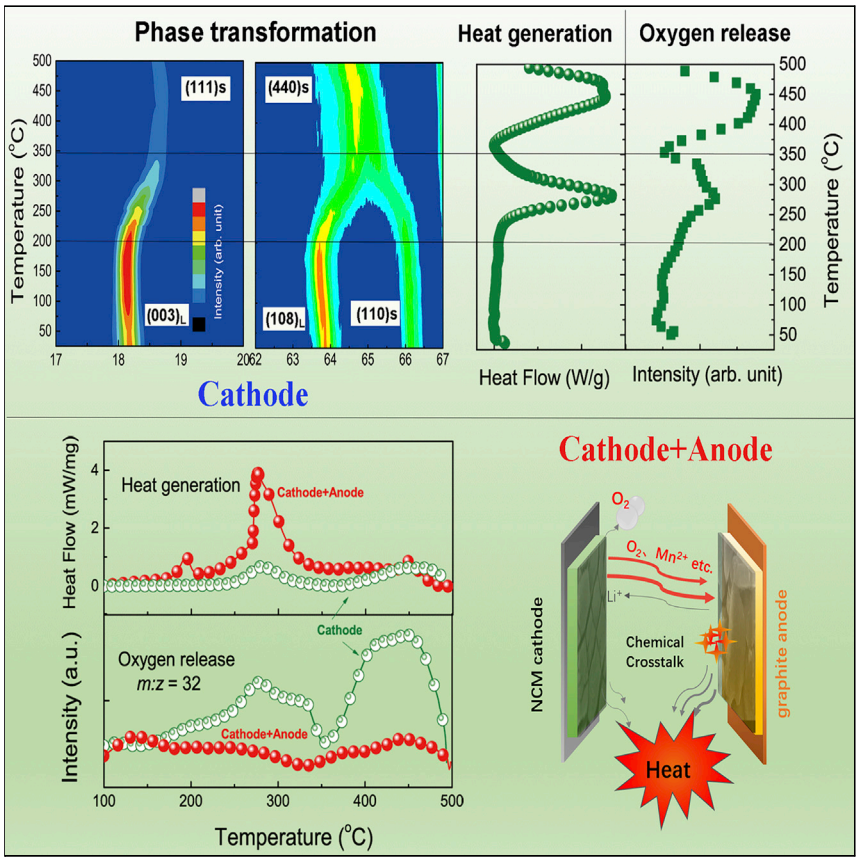

This article reports the thermal runaway mechanism of a 25-Ah large-format lithium-ion battery without internal short circuit induced by Joule heat. In this condition, chemical crosstalk is believed to be the mechanism. Specifically, cathode-produced oxygen is consumed by the anode with great heat generation. This finding is important for better design of LIBs to avoid thermal runaway via the optimization of all battery components.

Xiang Liu, Dongsheng Ren, Hungjen Hsu, ..., Xiangming He, Khalil Amine, Minggao Ouyang

amine@anl.gov (K.A.)
ouymg@tsinghua.edu.cn (M.O.)

HIGHLIGHTS

Thermal runaway of 25-Ah LIBs without internal short circuits is reported

Cathode-produced oxygen is consumed by the anode with heat generation

Chemical crosstalk is the hidden thermal runaway mechanism at high temperature

Cathode with inferior thermal stability may trigger the TR more intensively

Liu et al., Joule 2, 1–18
October 17, 2018
https://doi.org/10.1016/j.joule.2018.06.015

Please cite this article in press as: Liu et al., Thermal Runaway of Lithium-Ion Batteries without Internal Short Circuit, Joule (2018), https://doi.org/10.1016/j.joule.2018.06.015

Joule

CellPress

Article

Thermal Runaway of Lithium-Ion Batteries without Internal Short Circuit

Xiang Liu,[1,2] Dongsheng Ren,[1] Hungjen Hsu,[1] Xuning Feng,[1,3] Gui-Liang Xu,[2] Minghao Zhuang,[2,4] Han Gao,[2] Languang Lu,[1] Xuebing Han,[1] Zhengyu Chu,[1] Jianqiu Li,[1] Xiangming He,[3] Khalil Amine,[2,5,6,*] and Minggao Ouyang[1,7,*]

SUMMARY

We demonstrate herein that not only internal short circuiting, but also chemical crossover, is the mechanism behind thermal runaway that can occur in lithium-ion batteries due to abuse conditions. *In situ* experiments showed that during thermal runaway, the cathode releases oxygen by a phase transition, and this oxygen is consumed by the lithiated anode. The released highly oxidative gas reacts with reductive LiC_x with tremendous heat generation centered at 274.2°C with heat flow of 87.8 W g^{-1}. To confirm the proposed mechanism, we froze a battery undergoing the thermal runaway process by liquid nitrogen and subjected it to detailed post-test analysis. Our results revealed the hidden thermal runaway mechanism of chemical crossover between the battery components without a severe internal short circuit. These findings provide an important insight into the rational design of automotive lithium-ion batteries as well as solid-state batteries.

INTRODUCTION

With the explosive growth of portable electronic devices and electric vehicles, there is a strong need for lithium-ion batteries that have higher energy density and improved safety.[1–3] Recently, the development of nickel-rich cathodes and silicon/carbon anodes has pushed the energy density to a higher level[4–6]; however, battery safety is still a major concern. The most catastrophic failure mode of a lithium-ion battery is thermal runaway (TR), which should be avoided at all costs. This condition can be caused by overcharging, internal cell short circuiting, and vehicle collision. During TR, a chain reaction may happen with tremendous heat generation.[7–9] To understand the TR mechanism, past researchers have investigated the thermal response of the individual battery components, including the cathode,[10–13] anode,[3,14,15] electrolyte,[13] and separator.[14–17]

For example, it was reported that separator shrinkage or an incomplete shutdown may inadvertently increase the current density, resulting in additional localized heating or even causing TR of the cell.[16–18] Preparing the separator with high thermal stability is thus one way to improve the battery safety. Roth et al.[19] reported that a lithium-ion battery with a ceramic separator could withstand an overcharge to 300% of the state of charge without an internal short circuit. Moreover, several investigators have developed a separator with new material or structure that has even better thermal stability. Freudenberg announced an ultra-thin ceramic polyethylene terephthalate (PET) non-woven separator, which remains stable up to several hundred degrees Celsius.[20] In addition, Miao et al. reported a polyimide (PI) nanofiber separator that is thermally stable up to 500°C.[21] However, the

Context & Scale

With the explosive growth of portable devices and electric vehicles, there is an urgent need for safer Li-ion batteries (LIBs) with even higher energy density. The most catastrophic failure mode of LIBs is thermal runaway (TR) accidents; while TR only happens occasionally, it is a serious threat for the battery user and people nearby. In this paper, the mechanism behind TR without internal short circuiting is reported for the first time. A polyethylene terephthalate ceramic separator was used in battery tests to exclude the occurrence of an internal short circuit that is inducing Joule heat. Test results indicated that chemical crosstalk between the cathode and anode is the hidden mechanism that triggers TR, during which cathode-released oxygen is consumed by the lithiated anode, with a heat release rate of 87.8 W/g. The results advance understanding of the complicated TR mechanism in high-energy-density LIBs and should help in their future design.

Please cite this article in press as: Liu et al., Thermal Runaway of Lithium-Ion Batteries without Internal Short Circuit, Joule (2018), https://doi.org/10.1016/j.joule.2018.06.015

question remains: do those highly stable separators really guarantee the safety of the batteries?

Regarding the contribution of anode and cathode, Inoue and Mukai[22] announced an independent function in triggering the TR. They found that the anode's exothermic reaction dominates in a cell with a normal nickel-manganese-cobalt (NMC) cathode, but the cathode's energy release dominates in a cell with a nickel-cobalt-aluminum oxide cathode. However, this study did not take into account the contribution of an internal short circuit being induced by Joule heat and the interaction between the battery components. In short, the TR mechanism is still controversial, and to achieve optimized storage and safety properties of lithium-ion batteries, systematic analysis of both the cell level and the raw material level is needed.

Here, we investigate the TR mechanisms of an automotive battery on both the cell level and the material level. A large-format pouch cell battery (25 Ah) with graphite anode, single-crystal layered lithium transition metal oxide cathode ($LiNi_{0.5}Mn_{0.3}Co_{0.2}O_2$, NMC), and a PET/ceramic non-woven separator was used. The TR characterization was conducted by an electric vehicle accelerating rate calorimeter (EV+ ARC). During the TR ignition, the battery voltage was maintained at more than 2.0 V without an internal short circuit, which is consistent with the melting temperature of the PET nanofiber (about 257°C). Our research revealed that the TR of the cell is not ignited by heat generation of the internal short circuit, but the chemical crosstalk between the cathode and anode plays an important role. To illustrate the formation and evaluation of the TR process, we carefully analyzed the gas release, phase transformation, and heat generation of the cathode with and without the anode by various *in situ* and *ex situ* techniques.

Our findings have enriched the knowledge of the complicated lithium-ion battery TR mechanism. The results indicate that the safety design of automotive batteries should be conducted by an analysis at a system level, rather than by only improvement of a single material. For example, as discussed in this article, the chemical crosstalk may lead to TR, even though a thermally stable separator is being used to prevent internal short circuiting. The results also have implications for the design of all-solid-state batteries (ASSBs), which use solid ceramic or polymeric electrolytes with no separators. A safety benefit of ASSBs is usually claimed by researchers; however, as revealed herein, if the cathode releases oxygen that can react with the anode, there would be a serious safety issue. In our opinion, the safety of ASSBs should be carefully verified in both coin cells and large-scale automotive cells. By understanding the TR mechanism, especially the trigger point (threshold), we could determine the upper-limit temperature tolerance of the batteries and use that information to build a thermal model, design an improved battery management system, and develop TR prevention strategies to keep the battery temperature from exceeding this specific value.

The results are presented and discussed in two parts, the first dealing with the full battery ARC test and the second with a detailed post-test analysis of the battery components. First, by using the EV+ ARC, the self-heat onset temperature (T_1), TR temperature (T_2), and the maximum temperature (T_3) reached during TR were characterized in an adiabatic process. We note that T_2 is even lower than the thermal shrinkage temperature of the separator, which means that the battery's catastrophic TR happens without a large-scale short circuit caused by separator failure. This TR phenomenon without an internal short circuit is reported for the first time. To understand the detailed heat generation of the battery, we studied the heat flow of

[1]State Key Laboratory of Automotive Safety and Energy, Tsinghua University, Beijing 100084, China

[2]Chemical Sciences and Engineering Division, Argonne National Laboratory, Argonne, IL 60439, USA

[3]Institute of Nuclear and New Energy Technology, Tsinghua University, Beijing 100084, China

[4]Department of Chemical and Biological Engineering, Hong Kong University of Science and Technology, Clear Water Bay, Kowloon, China

[5]Institute for Research & Medical Consultations, Imam Abdulrahman Bin Faisal University, PO Box 1982, Dammam 31441, Saudi Arabia

[6]Materials Science and Engineering, Stanford University, Stanford, CA 94305, USA

[7]Lead Contact

*Correspondence: amine@anl.gov (K.A.), ouymg@tsinghua.edu.cn (M.O.)

https://doi.org/10.1016/j.joule.2018.06.015

Please cite this article in press as: Liu et al., Thermal Runaway of Lithium-Ion Batteries without Internal Short Circuit, Joule (2018), https://doi.org/10.1016/j.joule.2018.06.015

different components (anode, cathode, electrolyte, and their combinations) by differential scanning calorimetry (DSC). *In situ* high-temperature X-ray diffraction (XRD) was also applied to determine the cathode phase-transition behavior during heating and thermal decomposition. More importantly, to reveal the oxygen release of the charged electrodes, simultaneous thermal analysis (STA) combining thermogravimetry and DSC (TG-DSC) was coupled with mass spectrometry (MS) to simultaneously monitor the heat generation, weight loss, and gas release. Finally, to further confirm the proposed mechanism, we froze the battery at 206°C by liquid nitrogen purge just before the TR ignition. Post-test analyses were then conducted, including scanning electron microscopy (EM), inductively coupled plasma atomic emission spectroscopy (ICP-OES), and X-ray photoelectron spectroscopy (XPS) with plasma etching.

RESULTS AND DISCUSSION

Cycling Performance of SC-NMC532/Graphite Battery with a PET/Ceramic Separator

A 25-Ah large-format lithium-ion battery with energy density around 170 Wh/kg for electric vehicles was adopted in this study to understand the TR mechanism. The basic information about the battery chemistry is summarized in Table S1 (see Supplemental Information). Besides the high capacity, this battery has two other advantages compared with ordinary lithium-ion batteries. The first advantage is that it can use the PET/ceramic non-woven separator. A 20-μm thick separator was purchased from Freudenberg and used without further treatment. This separator paved the way for investigating the battery TR mechanism by eliminating the effect of domestic Joule heating caused by an internal short circuit while the separator was breaking down.[23] Another advantage is that the single crystal (SC)-NMC532 cathode can be used. The SC-NMC cathode is regarded as one of the promising cathode candidates with a high capacity,[24] caused by the larger crystal size of the SC-NMC532 leading to a higher tap density compared with that of the common polycrystalline cathode.

The cycling and rate performance of the battery are shown in Figure 1. The initial discharge capacity was 25.04 Ah, and the capacity remained high at 24.08 Ah after the 292nd cycle, with capacity retention around 96%. The deliverable discharge capacity at 1/5C, 1/2C, 1C, 2C, 3C, 4C, and back to 1/2C was 24.9, 24.0, 23.1, 22.4, 22.0, 21.5, and 24.1 Ah, respectively. These data indicate stable long-term cycling as well as good rate performance of the battery. The dQ/dV charge and discharge plots of the cell at 1/5C are shown in Figure S1. The electrochemical redox reaction is essentially the same for the polycrystalline NMC 532 and the SC-NMC cathode, with the oxidation and reduction pair peaking at 3.56 V and 3.68 V versus Li/Li^+.

Thermal Runaway of Lithium-Ion Batteries with Ceramic Separator and PET/Ceramic Separator

The TR properties of lithium-ion batteries were measured by the EV+ ARC system. Along with the cell temperature, the open-cell voltage and cell impedance were collected during the testing. The TR test procedure was conducted by following our previous experimental approach,[9] with typically two batteries mounted together. In addition, the impedance of the cell was obtained by a battery internal resistance recorder at a constant AC frequency of 1 kHz.

Figure 2 shows the temperature obtained during the self-heating and TR process. To enable better understanding of the TR phenomenon, T_1, T_2, and T_3 are marked in Figure 2. As evident in the figure, T_1 is located at 115.2°C, and is the onset

Please cite this article in press as: Liu et al., Thermal Runaway of Lithium-Ion Batteries without Internal Short Circuit, Joule (2018), https://doi.org/10.1016/j.joule.2018.06.015

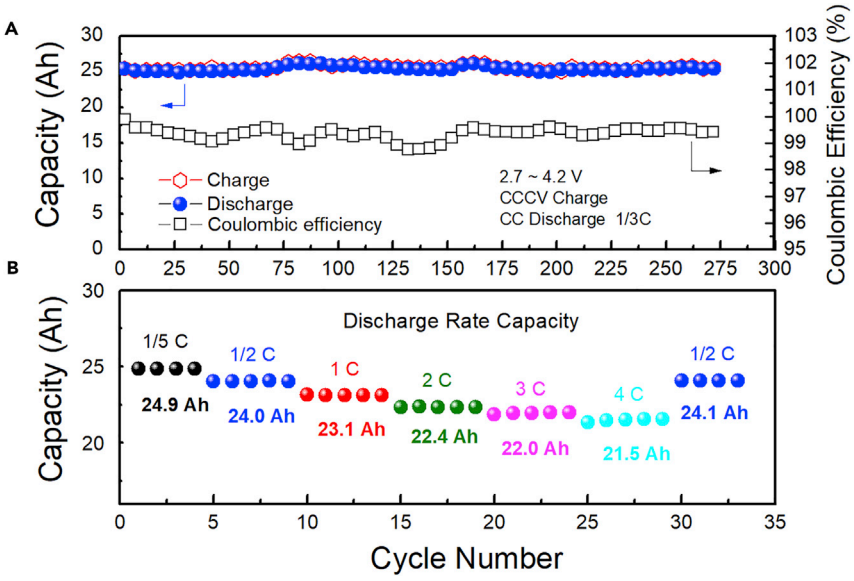

Figure 1. The Basic Performance of the Automotive Battery

(A) The cycling performance with coulombic efficiency.

(B) The rate performance.

temperature of the battery self-heating process. After each heat-wait-seek process, the ARC system checks if the temperature increase rate of the battery reaches the pre-set target, which is 0.02°C/min. If it does not, there is another heating stage with precisely controlled increases of 5°C per step. As shown in the inset of Figure 2, there are 15 heating steps before T_1. Thereafter, the self-heating reaction of the battery begins. The ARC system enters an exothermal process and provides an adiabatic environment. During this stage, the chemical parasitic reactions[9,25] caused by the increasing temperature are recorded precisely. It is known that at first, the solid-electrolyte interphase (SEI) of the anode decomposes;[26,27] thus the released fresh lithiated anode surface may react with the electrolyte to form a new SEI layer with heat generation. The metastable components of the SEI decompose at this stage. Bodenes et al.[28] confirmed that after high-temperature cycling, the SEI reformation can lead to the carbonate species disappearing and the inorganic layer on the anode surface increasing.

The exothermal stage of the battery begins after T_1. During this stage, the ARC system can maintain an adiabatic environment inside the battery, with control to 0.05°C. As mentioned in our previous work,[26] various parasitic reactions occur one after another, forming a chain reaction. As a result, the exothermic reactions can drive a continuous battery temperature rise continuously until catastrophic TR. The onset temperature of the TR is marked as T_2. At this critical point, the battery temperature increases exponentially. The temperature T_2 is defined as the point where the heating rate reaches 1°C/s, which is 231°C in this case.

To gather more information, we recorded a video during the TR process through a camera window open in the side wall of the ARC chamber, as shown in Videos S1 and S2. The video recording configuration is illustrated in Figure S2. As shown in Video S2, a severe exothermal reaction happened at T_2 and a tremendous amount of smoke poured out of the battery. The smoke was so heavy that it blocked the camera lighting in just a few seconds. In addition, significant battery volume expansion

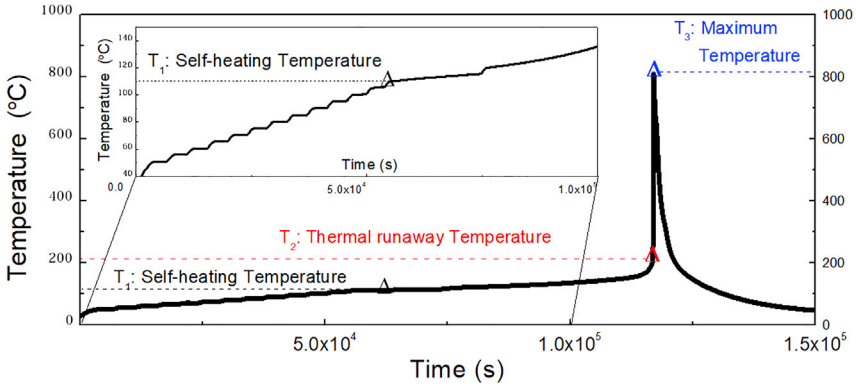

Figure 2. Thermal Runaway Temperature Plots of 25-Ah SC-NMC532/Graphite Cell Measured by EV+ ARC

The inset photo illustrates the data for the self-heating process up to 10^5 s.

was observed during the self-heating process as shown in Video S1. It revealed that the exothermic parasitic reaction was caused by gas production. After T_2, the battery temperature increased sharply and reached the maximum temperature T_3 at 815°C in just a few seconds.

Traditionally, via the ARC test the temperature is the only observed parameter to reveal the battery's exothermal reaction and the TR phenomenon. However, the temperature alone is not enough to describe the comprehensive cell chemistry. For example, the internal short circuit of the battery is reported to have vital importance to the battery safety, and may even ignite the TR.[29,30] As a result, battery voltage and the internal resistance are determined with an external battery resistance tester during the entire ARC test. The battery AC impedance (1 kHz) was obtained *in situ* during the TR process.

Plots of the temperature rate, cell voltage, and resistance versus the temperature are shown in Figure 3. In Figure 3A, the turning point of the temperature increase rate is located around 160°C, after T_1. As described earlier, when the existing SEI layer breaks down, the fresh lithiated anode surface may react with the electrolyte to accelerate the exothermic progress. In addition, the $LiPF_6$ in the electrolyte may start to decompose during this stage.[22,27,31,32] Note that both the SEI and electrolyte decomposition may produce gas, consistent with what can be observed from Video S1.

From Figure 3A, it is important to note that the cell voltage is maintained above 2.0 V during the TR process, indicating that the battery goes to a TR without a severe internal short circuit. To the best of our knowledge, this is the first report of a TR without a cell internal short circuit. To confirm this result we repeated the experiment, the data of which are shown in Figure S3. The preservation of the cell voltage is mainly due to the PET/ceramic separator. Compared with the traditional polypropylene (PP) or polyethylene (PE) separator, the PET/ceramic separator is more stable at high temperature. It showed little shrinkage after 250°C storage for 30 min, as evident in Figure 4 and Table S2, and even at 210°C storage for 13 hr, as shown in Figure S7. Note that the cell voltage drops to zero only when the temperature increase rate reaches the maximum of 20.1°C/s, as shown in Figure 3C. This may reveal the TR propagation process inside the pouch cell between the anode and cathode layers. As all the layers are connected in parallel inside the battery with zigzag

Please cite this article in press as: Liu et al., Thermal Runaway of Lithium-Ion Batteries without Internal Short Circuit, Joule (2018), https://doi.org/10.1016/j.joule.2018.06.015

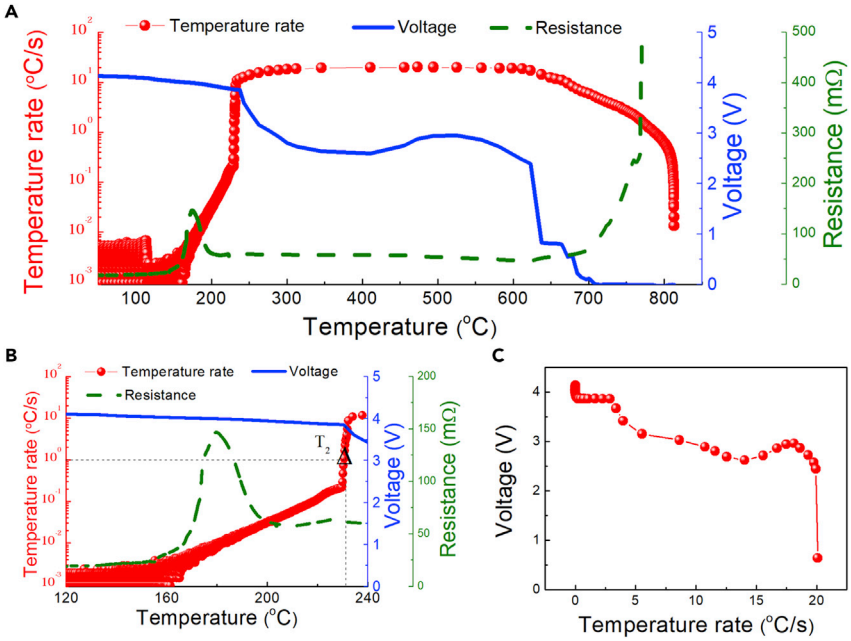

Figure 3. Thermal Runaway Characterization of 25-Ah SC-NMC532/Graphite Cell

(A) Temperature rate, cell voltage, and internal resistance versus absolute temperature during TR process.

(B) Segment of Figure 2A focusing on the internal resistance before TR.

(C) Relationship between the cell voltage and temperature rate during the TR process.

stacking, the cell voltage drops to zero only when the last anode/cathode pair goes into TR. Finegan et al.[30] have also reported the observation of TR propagation between the anode and cathode layers.

The cell internal resistance obtained during the TR process is plotted by the dashed line in Figures 3A and 3B. The initial resistance is 19.2 mΩ, including 9.8 mΩ from the connecting wire. Thus, the battery resistance obtained by the tester is 9.4 mΩ, which is consistent with the hybrid pulse power characterization shown in Figure S4. There are generally four stages of the resistance change during TR. At first, before 145°C, the resistance increases at a very slow rate to 22.1 mΩ. This slow increase occurs because the parasitic reaction is limited, since the original cell chemistry changes little during this stage. In stage II from 145°C to 175°C, the resistance proportionally increases to 143.3 mΩ. There are three main reasons for this large increase. First, as shown in Video S1, the pouch cell swelled tremendously between 123°C and 141°C, then at around 145°C the cell burst under high pressure. The bursting of the pouch cell may have accelerated the electrolyte's evaporation, thus leading to the sharp increase in resistance. Second, the cathode impedance growth may also contribute to the cell resistance increase, as indicated by the Xiong et al.[33] report that the cathode impedance grows significantly after 60°C storage. Third, the decomposition of the metastable outer layer of the SEI can lead to the inorganic layer increase of the anode surface,[27,28] thus reducing the ion conductivity. The battery swelling, the pouch bag bursting, and the gas venting temperature are pointed out in Figure S5.

Surprisingly, in stage III the cell resistance decreased from 143.3 mΩ to 56.5 mΩ between 180°C and 231°C before TR. The decreased resistance may have been caused

Please cite this article in press as: Liu et al., Thermal Runaway of Lithium-Ion Batteries without Internal Short Circuit, Joule (2018), https://doi.org/10.1016/j.joule.2018.06.015

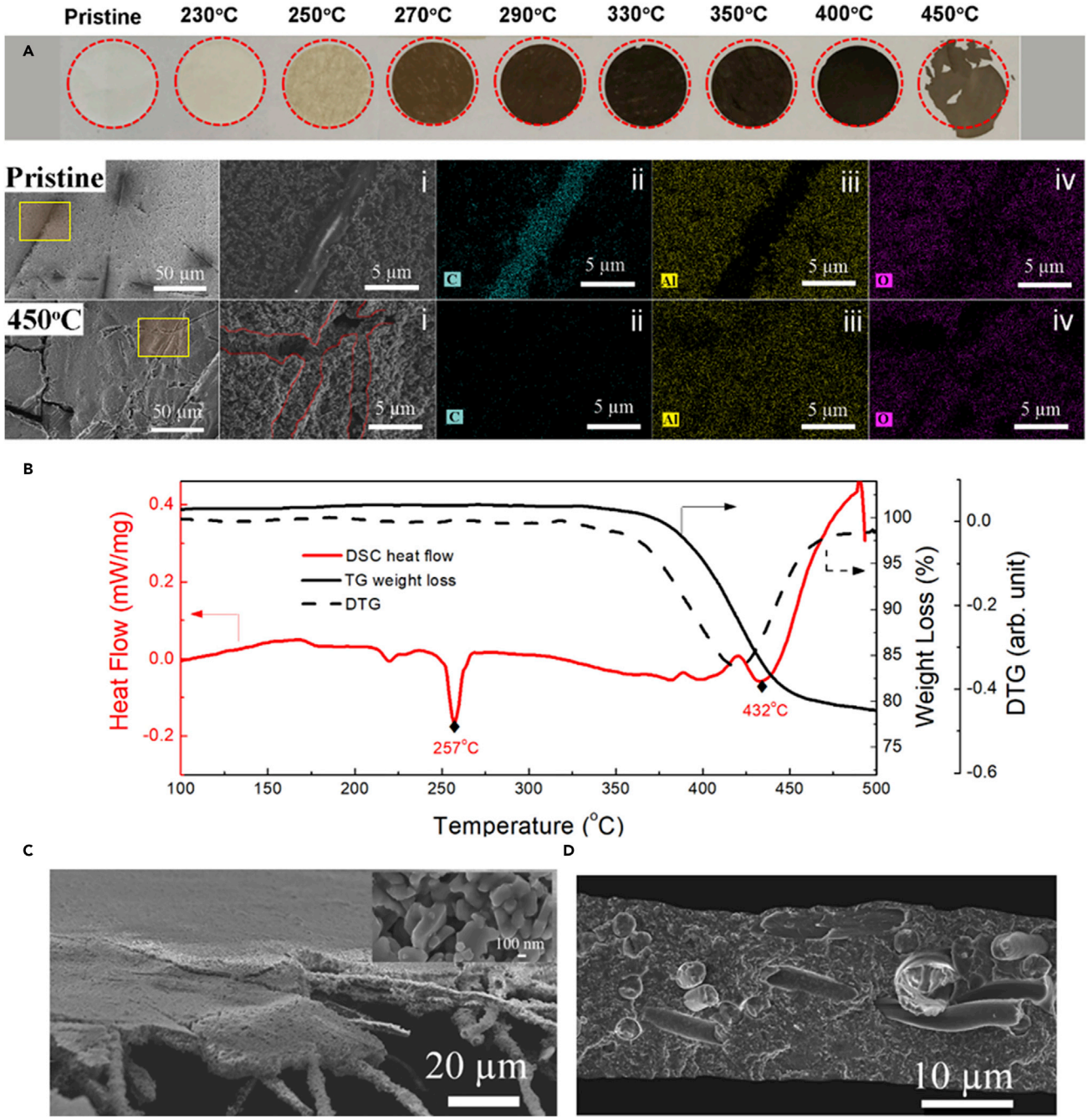

Figure 4. Structure and Thermal Properties of PET/Ceramic Non-woven Separator

(A) Images of the PET/ceramic separator after thermal stability test from room temperature (pristine) to 450°C; below are photos of the scanning EM morphology and element mapping of the pristine and 450°C sample.

(B) DSC heat flow and TGA weight loss of the separator from room temperature to 500°C at 10°C/min.

(C) Scanning EM from surface tilt view of the PET/ceramic non-woven mat separator; the inset is an enlarged scanning EM photo of Al_2O_3 surface.

(D) Cross-sectional view of the separator; PET non-woven fiber surrounded by Al_2O_3 nanoparticles (UV-epoxy is used to embed the cross-sectional sample).

by the transition of the metal dissolution, which was confirmed later by XPS analysis of the battery after liquid nitrogen cooling. In addition, the decomposition of the $LiPF_6$ salt in the electrolyte and the subsequent possible reactions may also lead to the resistance change.[25,31] At the last stage the battery resistance dropped

Please cite this article in press as: Liu et al., Thermal Runaway of Lithium-Ion Batteries without Internal Short Circuit, Joule (2018), https://doi.org/10.1016/j.joule.2018.06.015

sharply after the TR was ignited, then bounced back to around 50 mΩ, which was maintained for a few seconds until the voltage dropped to zero. After the voltage dropped, the cell resistance increased sharply to 1,011.2 mΩ, which may be attributed to the separator breakdown and entire battery failure.

As mentioned above, the separator plays a vital role in protecting the cell from an internal short circuit before TR. To confirm the thermal stability and the structure of the PET/ceramic separator, we used hot box storage with post-test analysis, including thermogravimetric analysis (TGA), energy dispersive X-ray spectroscopy (EDX) mapping, DSC, and scanning EM. As shown in Figure 4A, the PET/ceramic separator was cut into a circle with a diameter of 14 mm and left in the hot box for 30 min at different target temperatures from 210°C to 450°C. The shrinkage rates as a function of temperature are summarized in Table S2 and Figure S6. At the point of TR ignition at 231°C, the observation of only 1.2% shrinkage explains why an internal short circuit did not happen before TR (see also Figure S7 for results from 13-hr, 210°C storage). The DSC and TG analyses are shown in Figure 4B. The first obvious endothermic peak of the separator is located at 257°C by DSC, while there is no weight loss at this stage indicated by TG. This endothermic reaction can be attributed to the PET melting. However, the following endothermic peak, at around 432°C, comes with an obvious weight loss due to PET degradation. The separator turns black due to the PET melting, then becomes pure white after 450°C storage, whereby PET degradation leaves only ceramic particles.

To view the failure process of the PET/ceramic separator after melting (also after TR), Figure 4A shows the scanning EM image with EDX mapping of the pristine separator and the separator after 450°C storage. Figure 4C shows the scanning EM tilt image of the PET/ceramic separator, and the inset image reveals the morphology of the surface ceramic layer. As shown, the non-woven PET nanofiber is embedded in the ceramic nanoparticles rather than in a simple double-sided ceramic coating. The cross-sectional image of the separator in Figure 4D reveals that the separator is around 19.5 μm in thickness, with the PET nanofiber thickness being from around 1.8 μm to 5.8 μm.

The cell voltage and separator thermal stability results both confirmed that a severe internal short circuit did not trigger the TR. Therefore, there must be other factors besides an internal short circuit that ignite and cause the abrupt temperature increase during TR.

Thermal Stability of Each Component of Lithium-Ion Battery

For a better understanding of the TR ignition, it is necessary to have detailed knowledge about the cell chemistry, thermal response, and phase transition of all battery components. In this regard, the reaction chemistry between the electrode materials and the electrolyte components has been studied step by step with DSC, as shown in Figure 5. For the DSC measurement, the 25-Ah battery was charged to 4.2 V, then disassembled in an argon-filled glovebox with controlled oxygen and water concentration. Before scratch-off from the current collector, both the cathode and anode electrodes were rinsed with dimethyl carbonate (DMC) solution several times to remove the residual electrolyte. Typically, 9.4 mg charged electrode powder with 3 μL of electrolyte (1 M $LiPF_6$ in EC/DMC/EMC 1:1:1 in volume) was placed into a hermetic aluminum pan with a hole for the DSC measurement.

Figures 5A and 5B show the DSC heat-flow profiles of charged electrodes without and with the electrolyte. At first, to eliminate the influence of the electrolyte, dry electrodes were subjected to DSC, the results of which are shown in Figure 5A.

Please cite this article in press as: Liu et al., Thermal Runaway of Lithium-Ion Batteries without Internal Short Circuit, Joule (2018), https://doi.org/10.1016/j.joule.2018.06.015

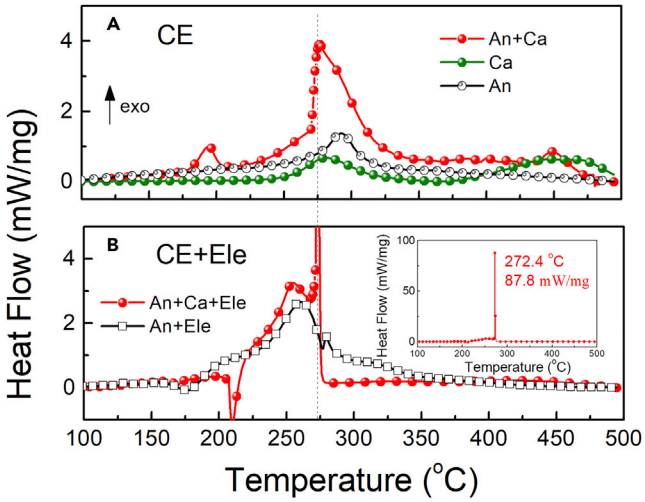

Figure 5. The Heat Generation of the Charged Battery Components by DSC Measurements

(A) Charged electrode (CE) without electrolyte.

(B) Charged electrode with electrolyte.

An, anode; Ca, cathode; Ele, electrolyte; CE, charged electrode.

The lithiated anode exhibits one exothermic peak at 292.5°C with heat flow and ΔH of 1.4 W g^{-1} and 304 J g^{-1}, respectively. These values are consistent with previous reports[15,34] and are believed to be associated with the LiC_x reaction with the binder used. The delithiated cathode alone exhibits two exothermic peaks at 279°C and 444°C, with ΔH of 108 J g^{-1} and 148 J g^{-1}, respectively. However, when mixing the cathode and anode, as shown by the red dotted line of Figure 5A, the heat generation (integrated peak area) increased tremendously to 770 J g^{-1}, which almost triples the value of the anode alone and is seven times larger than the cathode alone. In addition, the heat flow increased from 1.4 W g^{-1} to 3.8 W g^{-1}. The DSC profiles with electrolyte are shown in Figure 5B. With the presence of the electrolyte, the anode exothermic reaction starts earlier, with the ΔH value and peak intensity rising to 956 J g^{-1} and 2.4 W g^{-1}, respectively, at 261°C. Nevertheless, when combining the anode and cathode with the electrolyte, the exothermic reaction increased alarmingly from 2.4 W g^{-1} at 270°C to 87.8 W g^{-1} at 272°C, with a ΔH value of 1,377 J g^{-1}. The DSC results for the cathode and separator with the electrolyte are shown in Figure S8. They indicate that the electrolyte has little effect on those two components. Note that regardless of the electrolyte, mixing the anode and cathode together will produce an abrupt increase in heat release.

To reveal the reason for the peak intensity increment and TR mechanism of the automotive battery, we propose a chemical crosstalk reaction between the anode and cathode. To verify this proposal, we applied liquid nitrogen cooling to harvest the electrode materials just before TR and then conducted temperature-resolved XRD, *in situ* STA-MS, and other post-test analyses (scanning EM, XPS, and ICP-OES).

Chemical Crossover between the Electrodes at Elevated Temperature

Recently, Xiong et al.[33] reported cathodic CO_2 production and further reaction with the anode at 60°C, and Michalak et al.[35] proposed that nickel reduction plays a profound role in CO_2 generation on the cathode surface. However, the effect of the most dangerous gas, which is oxygen, has not been investigated in a systematic fashion. It is widely reported that the delithiated NMC cathode is not stable at a high temperature[10,36–38] (typically between 150°C and 300°C, depending on the

Please cite this article in press as: Liu et al., Thermal Runaway of Lithium-Ion Batteries without Internal Short Circuit, Joule (2018), https://doi.org/10.1016/j.joule.2018.06.015

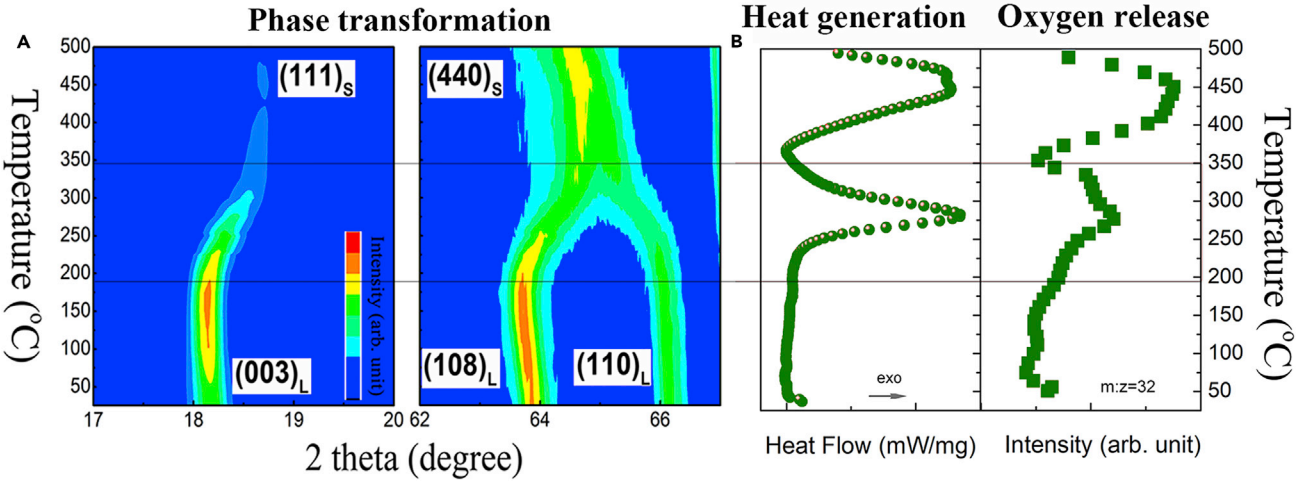

Figure 6. Phase Transformation, Heat Generation, and Oxygen Release of Charged Cathode Materials

(A) Contour plots of the time-resolved XRD patterns at selected 2θ ranges and temperatures from 25°C to 500°C.

(B) *In situ* heat generation and oxygen release at different temperatures determined by DSC and TGA-MS system.

delithated state and Ni concentration). This instability is caused by phase transformation and accompanied with lattice oxygen release. We are proposing the chemical crosstalk between the cathode oxygen and anode as the reason for full-cell TR ignition.

Figure 6 shows the phase transformation, heat generation, and oxygen release profiles of the charged cathode as a function of temperature from 25°C to 500°C. In Figure 6A, the phase transition is shown in a temperature-resolved XRD with an *in situ* heating tool. (The CO_2 and H_2O gas comparison is shown in Figure S9, and the original XRD plots with different temperatures are shown in Figure S10.) The charged cathode is prepared in the same manner as for the DSC test. As shown, the SC-NMC532 cathode starts the phase transition from a layered structure to a spinel structure at around 200°C, and the phase change is complete at about 350°C with the temperature window being 150°C. Compared with the polycrystalline NMC532 cathode reported by Bak et al.,[10] the phase transition starts earlier and has a larger transforming temperature window.

The DSC heat generation and MS oxygen gas (m/z = 32) characterization versus temperature are shown in Figure 6B. Note that both the heat generation and oxygen release coincide with the phase transition. As shown, the first exothermic peak starts at 200°C, followed by the phase transition, and the corresponding oxygen release starts at 150°C. The heat generation and oxygen release peaks are both centered at 276°C, indicating that a severe phase transition is under way at this temperature. Since there is no internal short circuit induced by Joule heat, this oxygen release is crucial to understanding the TR ignition at the cell level. The oxygen can diffuse through the separator, then react with the highly reductive Li_xC anode. A mixture of cathode/anode powder was analyzed by STA-MS. The heat generation and oxygen release profiles of the cathode alone and the cathode/anode mixture are compared in Figure 7. As shown in the MS (m/z = 32) plots for the cathode/anode mixture in Figure 7A, the first oxygen release peak of the cathode at 276°C visually disappeared, indicating that the oxygen was consumed by the anode. This is also confirmed by the weight loss comparison, as shown in Figure S11. The cathode weight loss is 2.8% at 276°C, much larger than that of the cathode/anode mixture,

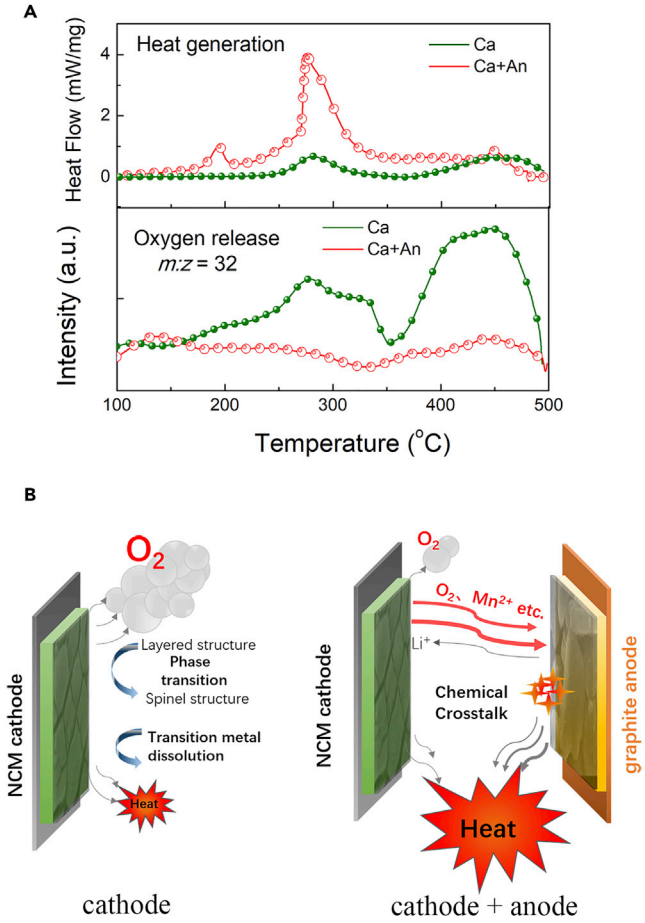

Figure 7. Chemical Crosstalk between the Charged Cathode and Anode

(A) Charged cathode alone exhibits strong oxygen release peak while the mixture of cathode/anode releases virtually no oxygen but has sharp heat generation enhancement at the same temperature range.

(B) Illustration of proposed chemical crosstalk process between cathode and anode.

which is only 0.7%. Consequently, because of the oxygen release the exothermic peak for the cathode alone centered at 276°C increased over seven times. The resulting heat generation was 770 J g^{-1} for the cathode/anode mixture but only 108 J g^{-1} for the pure cathode.

A schematic representation of this chemical crosstalk between the cathode and anode and the resulting heat generation boost is shown in Figure 7B. The charged cathode alone can produce oxygen at an elevated temperature because of a phase transformation, with limited heat generation. However, when mixed with the anode, the boost of heat generation occurs. At this stage, with the oxygen gas, reactive agent, and the high temperature, the exothermic TR occurs intensively from inside the battery. If TR happens, even a liquid nitrogen purge will not stop the reaction effectively. As shown in Figure S12, the battery still goes into TR after the liquid nitrogen purge at 218°C. Therefore, to guarantee the safety of the battery system for electric vehicles, thermal management strategies must be implemented before a catastrophic TR happens; otherwise, if TR happens, even a liquid nitrogen purge with the maximum heat dissipation cannot stop the fire because the oxygen is provided from the NMC cathode inside the battery.

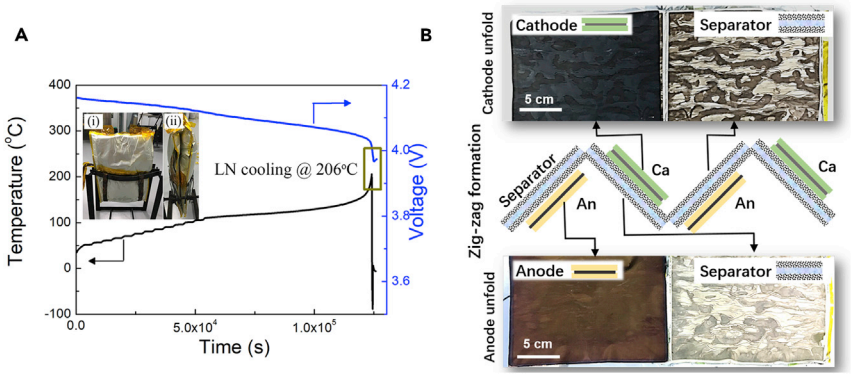

Figure 8. Liquid Nitrogen Freezing of Battery before Thermal Runaway

(A) Temperature and voltage curves of TR at 206°C obtained by liquid nitrogen purge. Inset shows the front view (i) and side view (ii) of the lithium-ion batteries after LN cooling.

(B) Configuration of zigzag-type stacking and the images of inside cathode/anode with separator after LN cooling at 206°C.

Liquid-Nitrogen-Ceased Thermal Runaway and Post-test Analysis

Although liquid nitrogen (LN) cannot cool down the battery immediately after TR, it is effective before TR. By LN freezing, the cathode and anode materials of the battery can be preserved for post-test analysis. By this method, we successfully ceased the reaction before TR at 206°C, as shown in Figure 8. The battery temperature stops increasing immediately at 206°C after the LN purge and then drops to around −100°C. The inset images of Figure 8A show the front view and side view of the lithium-ion batteries after LN cooling, which shows that the batteries are well preserved without TR; however, the pouch bag has already burst from the side. After cooling, the whole battery was carefully disassembled in a glovebox, as shown in Figure 8B. By disassembling the battery before TR, we again confirmed that the PET/ceramic separator is well preserved with no visual holes or damage, which is the key factor in maintaining the cell voltage and preventing an internal short circuit. An optical image showing the integrity of the separator is presented in Figure S13. Moreover, to confirm that the separator can still work to prevent ionic leakage before TR, we constructed coin cells by using the harvested separator. The cycling performance of one of the coin cells is shown in Figure S14. In addition, Figure 8B shows obvious black stripes on the cathode surface and the separator nearby. However, the lithiated anode shows no noticeable change. To gain more insight into the chemistry change of the electrodes before the TR, we conducted post-test analysis, including morphology and element composition characterization. The results are shown in Figures 9, S15, and S16.

The scanning EM images in Figure 9A show a morphology comparison between the pristine charged cathode and the LN-frozen cathode at 206°C. The surface of the pristine charged cathode is clean and smooth with no obvious surface impurity, while the LN-frozen cathode displays a rough surface. Consider the black stripes on the cathode separator, which are highly related to the transition metal ion deposition, as can be deduced from Figure S16. The Ni, Mn, and Co cathode elements are detected on the anode surface. The phenomena of metal oxide dissolution, migration, and decomposition have also been reported by others.[39,40] Li and Lucht[41] observed lithium carbonate formation and decomposition on the cathode surface during the elevated temperature. Moreover, they observed that a higher temperature shifts the equilibrium, resulting in surface Li_2CO_3 dissolution, $Li_xPO_yF_z$ formation, and possible corrosion of the bulk metal oxide. The observed rough surface

Please cite this article in press as: Liu et al., Thermal Runaway of Lithium-Ion Batteries without Internal Short Circuit, Joule (2018), https://doi.org/10.1016/j.joule.2018.06.015

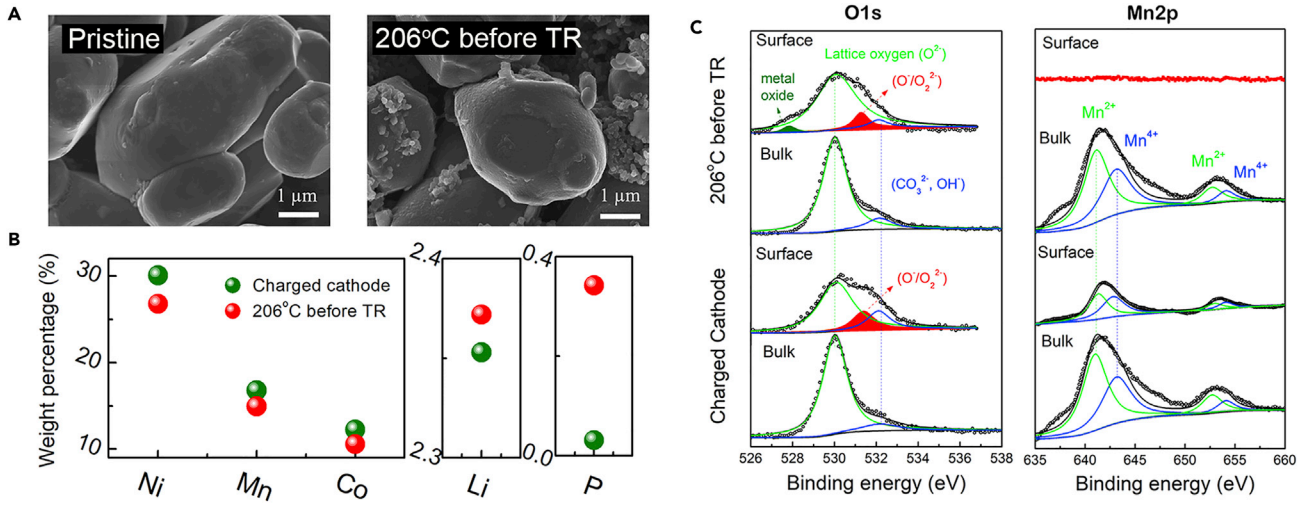

Figure 9. Post-test Analysis of the Battery after Freezing with Liquid Nitrogen

(A) Scanning EM surface image of the pristine charged NMC532 cathode and charged cathode before TR.

(B) Element composition of pristine charged cathode and charged cathode before TR by ICP-OES measurement.

(C) XPS analysis of pristine charged cathode and charged cathode before TR with plasma etching.

layer on the charged cathode before the TR may be related to the phosphorus layer formation, since phosphorous was detected on the cathode surface as shown in Figure S16. In addition, the ICP-OES characterizations were applied to the pristine charged cathodes and the cathodes before TR. For a pristine charged cathode, the weight percentage was determined to be 30.08 wt% Ni, 17.79 wt% Mn, and 12.25 wt% Co (Figure 9B). Thus, the mole ratio between Ni, Mn, and Co is 5.1:3.0:2.0, which is very close to the designed NMC532 composition. The lithium concentration in the pristine charged cathode was 2.35 wt%. However, the transition metal before TR are 26.79 wt% Ni, 14.95 wt% Mn, and 10.57 wt% Co, confirming that all transition metal ions undergo dissolution during the self-heating. Moreover, the observed phosphorous content increased more than 10-fold compared with the pristine cathode, from 0.03 wt% to 0.34 wt%. The chemical crosstalk between the cathode and anode may not only trigger the TR process by oxygen release but also may occur during the self-heating process.

The XPS profiles of the pristine charged cathode and LN-frozen cathode before TR are shown in Figure 9C. To obtain the depth element information, we applied Ar^+ plasma etching for 50 nm. At first, for the O1s peak, two major peaks appear for lattice oxygen (O^{2-}) and a surface organic compound and are centered at 530.0 eV and 532.2 eV, respectively. In addition, a surface (O^-/O_2^{2-}) peak is evident at 531.3 eV for the surface sample only, which is believed to be associated with the surface phase transition and thereby with released oxygen,[42] indicating that the phase transition mainly happened near the surface. In addition, a characteristic peak related to metal oxide, located at 527.8 eV, is observed in the TR sample surface frozen at 206°C (also shown in Figure S15). This finding confirmed the phase transition on the cathode with elevated temperature.

The XPS profile for the transition metal of Mn2p, shown in Figure 9C, indicates that for the sample before TR, the surface Mn signal completely disappeared on the cathode; however, it was detected on the anode and separator surface as shown in Figure S15. This suggests that the transition metal ions are subject to different reactions. More detailed work regarding the reaction pathways is warranted.

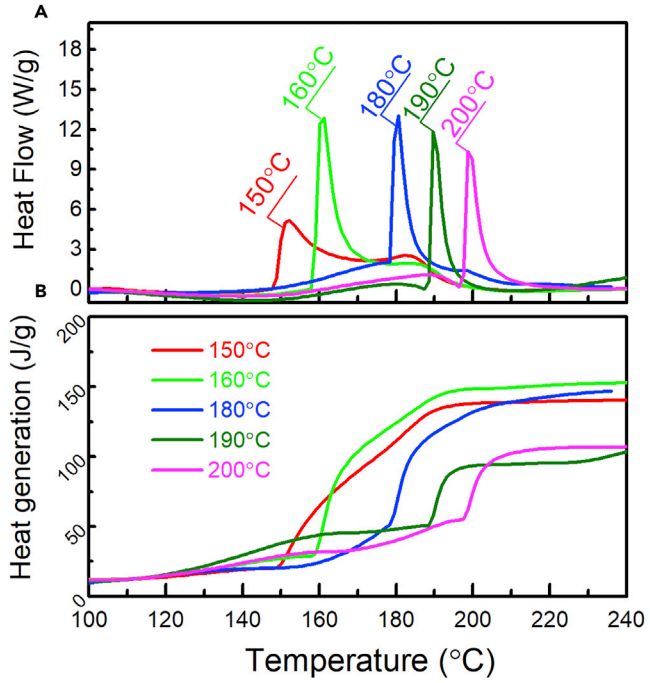

Figure 10. DSC Oxygen Induction Profiles on Charged Anode

(A) Oxygen induction as flow gas during DSC test of the charged anode at different temperatures.
(B) Total heat generation of the anode reaction with oxygen.

As discussed earlier, the Ni-rich NMC cathode has a higher capacity for lithium storage. However, this material suffers from inferior thermal stability.[5,10,43] As proposed, the chemical crosstalk, especially the cathode oxygen generation by phase change, plays a critical role in the battery TR process. The use of a Ni-rich cathode in a large-format lithium-ion battery may eventually affect the thermal response at the cell level. To simulate the oxygen generation of the Ni-rich cathode and the interaction of oxygen with the charged anode, we obtained DSC measurements with oxygen induction at different temperatures. The results are shown in Figure 10. The charged anode powder was prepared in the same manner as mentioned above for the normal DSC test without electrolyte. Pure oxygen was introduced as a gas flow at 40 mL/min. Target temperatures of 150°C, 160°C, 180°C, 190°C, and 200°C were used to simulate the oxygen release by cathode phase transition.

As shown in Figure 10A, the DSC heat generation increased immediately when the oxygen was introduced. This result confirmed that the released oxygen may react with the anode and produce fierce heat generation. Thus, if a Ni-rich cathode with inferior thermal stability is used, the abrupt heat generation may happen earlier. The integrated heat generation of all conditions is shown in Figure 10B for the temperature range from 50°C to 240°C. The heat generation for the oxygen induction condition of 190°C and 200°C is almost the same, which is around 105 J/g. However, with the earlier oxygen induction condition of 150°C, 160°C, and 180°C, the heat generation increases almost 43%, to 150 J/g. The results indicate that an inferior thermal stability cathode may not only trigger the TR process earlier but also produce more severe heat generation.

In sum, the chemical crosstalk is the hidden reason for the battery TR. In designing a safe high-energy-density automotive battery, the released oxygen from the cathode

Please cite this article in press as: Liu et al., Thermal Runaway of Lithium-Ion Batteries without Internal Short Circuit, Joule (2018), https://doi.org/10.1016/j.joule.2018.06.015

is the most critical factor to consider. If the cathode is vulnerable to high temperature, an advanced separator cannot guarantee the safety for a lithium-ion battery (or a battery with solid-state electrolyte). The rational design of the reliable high-energy-density battery needs careful verification at both the material level and automotive cell level.

Conclusions

To reach a better understanding of the TR mechanism due to abuse conditions with large-format lithium-ion batteries, we tested a thermally stable separator up to about 250°C in a 25-Ah lithium-ion battery. The stable separator eliminated the possibility of an internal short circuit induced by Joule heating generation. Our results revealed the TR mechanism as being driven by the chemical crossover between the cathode and anode without severe internal short circuit and voltage drop. At around 231°C, without an internal short circuit, the battery TR happened all at once. The TR mechanism of chemical crosstalk between the cathode and anode was thus proposed. We found that by a phase transition from layered to spinel structure, the charged cathode alone can release oxygen and produce a small amount of heat that peaks at around 276°C. However, when the cathode and anode are mixed together, the heat generation increased seven times with virtually no oxygen release. The cathode-released oxygen consumed by the anode thus triggered the TR process with a tremendous heat generation rate. These results may advance the understanding of the complicated lithium-ion battery TR mechanism and suggest that reliable design of automotive lithium-ion and solid-state batteries can be achieved by balancing the crosstalk among the cathode, electrolyte, and anode under ordinary operation and abuse conditions.

EXPERIMENTAL PROCEDURES

Accelerating Rate Calorimeter Test

The ARC tests were conducted with an EV+ ARC system purchased from Thermal Hazard Technology. For each ARC test, two fully charged 25-Ah batteries were combined with a thermocouple in between. The starting temperature was 40°C with a heating step of 5°C. The detected self-heating rate was 0.02°C/min and the waiting time was 40 min. Before the test, the ARC system was calibrated with a piece of Al placed in the chamber as a battery substitute, and a drift experiment was conducted after calibration to confirm the system reliability. The detailed test setups were similar to those discussed in our previous reports.[9] A TR video was taken by an external camera during the ARC test. The voltage recorded by a Neware battery test and the resistance were collected by a Tonghui TH2523A battery resistance tester with a consistent frequency of 1 kHz. Moreover, an external LN purge system was designed inside the ARC chamber to cool the sample inside.

Differential Scanning Calorimeter Test

The DSC measurement was conducted with a Netzsch DSC214 system. The temperature range was from room temperature to 500°C with a heating rate of 10°C/min. To obtain the charged electrode materials, we transferred a fully charged battery (Table S1) into an argon-filled glovebox and disassembled it carefully. The active materials on the current collector were immersed into a DMC solution and rinsed several times to ensure that a minimal amount of electrolyte remained in the electrode. Thereafter, the electrode was dried in the vacuum chamber for several hours. The NMC cathode and graphite powder were then removed carefully from the current collector with a surgical blade. Finally, the delithiated cathode and lithiated

Please cite this article in press as: Liu et al., Thermal Runaway of Lithium-Ion Batteries without Internal Short Circuit, Joule (2018), https://doi.org/10.1016/j.joule.2018.06.015

anode were ground carefully with an agate mortar to produce a uniform electrode powder, which was ready to use. A Concavus crucible/lid set was used for the DSC measurement. To reduce the oxygen and water contamination we added and sealed the electrode material in the glovebox, and made a hole on the lip just before the test. The amount of anode and cathode was 6.4 mg and 3.0 mg for each test, with around 3.0 μL of electrolyte.

Time-Resolved XRD and Post-test Analysis of Battery before Thermal Runaway

The time-resolved XRD measurement for the charged cathode was carried out by a Bruker D8 Avance XRD system, with an external direct heating component from room temperature up to 500°C. The charged cathode powder was prepared in the same manner as for the DSC measurement. The *in situ* STA-MS measurement was conducted by a Netzsch STA 449 F5 with a Netzsch QMS403D MS system, with the argon flow at 10°C/min from room temperature to 500°C. Scanning EM was conducted with a Zeiss Merlin field emission scanning electron microscope. The chemical compositions of the resulting powders were analyzed by inductively coupled plasma (Opima 8300, PerkinElmer). XPS measurement was conducted with a PHI Quantera SXM XPS system from ULVAC-PHI, with the X-ray spot diameter of 200 μm below 1.0×10^{-7} torr. An Ar^{+} plasma was used to etch the sample to determine the bulk material composition. The XPS results were calibrated with a C 1*s* emission peak of 284.6 eV.

SUPPLEMENTAL INFORMATION

Supplemental Information includes 16 figures, 2 tables, and 2 videos and can be found with this article online at https://doi.org/10.1016/j.joule.2018.06.015.

ACKNOWLEDGMENTS

This work is supported by the National Natural Science Foundation of China under grant no. U1564205, no. 51706117, and the International Science & Technology Cooperation Program of China under contract no. 2016YFE0102200. X.L. acknowledges financial support from the China Postdoctoral Science Foundation funded project nos. 2016M600088 and 2017T100075. The authors would like to thanks Hunan Li-Fun Technology for preparing the battery. The authors gratefully acknowledge the support from the US Department of Energy (DOE), Vehicle Technologies Office. Argonne National Laboratory is operated by DOE Office of Science by UChicago Argonne under contract no. DE-AC02-06CH11357. The authors also thank the support from Clean Vehicles, US-China Clean Energy Research Center (CERC-CVC2).

AUTHOR CONTRIBUTIONS

X.L. prepared and carried out the experiments. M.O. and K.A. conceived the project and provided the advice for preparing the experiment. D.R., H.H., X.F., and L.L. provided assistance during ARC and DSC tests. G.-L.X. and K.A. helped with the interpretation of time-resolved high-temperature XRD measurements. M.Z. and H.G. helped with the separator characterization. X.H. and Z.C. helped with the liquid nitrogen cooling system. J.L., X.H., L.L., and M.O. provided valuable advice while interrelating and preparing the manuscript. All authors contributed to the subsequent editing and improvement of the manuscript.

DECLARATION OF INTERESTS

The authors declare no competing interests.

Received: March 12, 2018
Revised: May 23, 2018
Accepted: June 19, 2018
Published: July 9, 2018

REFERENCES

1. Lu, L., Han, X., Li, J., Hua, J., and Ouyang, M. (2013). A review on the key issues for lithium-ion battery management in electric vehicles. J. Power Sources *226*, 272–288.

2. Sun, Y., Liu, N., and Cui, Y. (2016). Promises and challenges of nanomaterials for lithium-based rechargeable batteries. Nat. Energy *1*, 16071.

3. Chen, Z.H., Qin, Y., Ren, Y., Lu, W.Q., Orendorff, C., Roth, E.P., and Amine, K. (2011). Multi-scale study of thermal stability of lithiated graphite. Energ. Environ. Sci. *4*, 4023–4030.

4. Choi, J.W., and Aurbach, D. (2016). Promise and reality of post-lithium-ion batteries with high energy densities. Nat. Rev. Mater. *1*, 16013.

5. Rodrigues, M.T.F., Babu, G., Gullapalli, H., Kalaga, K., Sayed, F.N., Kato, K., Joyner, J., and Ajayan, P.M. (2017). A materials perspective on Li-ion batteries at extreme temperatures. Nat. Energy *2*, 17108.

6. Wang, Z., Yin, Y.P., Ren, Y., Wang, Z.Y., Gao, M., Ma, T.Y., Zhuang, W.D., Lu, S.G., Fan, A.L., Amine, K., and Chen, Z.H. (2017). High performance lithium-manganese-rich cathode material with reduced impurities. Nano Energy *31*, 247–257.

7. Feng, X., He, X., Ouyang, M., Lu, L., Wu, P., Kulp, C., and Prasser, S. (2015). Thermal runaway propagation model for designing a safer battery pack with 25Ah $LiNi_xCo_yMn_zO_2$ large format lithium ion battery. Appl. Energ. *154*, 74–91.

8. Guo, R., Lu, L., Ouyang, M., and Feng, X. (2016). Mechanism of the entire overdischarge process and overdischarge-induced internal short circuit in lithium-ion batteries. Sci. Rep. *6*, 30248.

9. Feng, X.N., Fang, M., He, X.M., Ouyang, M.G., Lu, L.G., Wang, H., and Zhang, M.X. (2014). Thermal runaway features of large format prismatic lithium ion battery using extended volume accelerating rate calorimetry. J. Power Sources *255*, 294–301.

10. Bak, S.M., Hu, E., Zhou, Y., Yu, X., Senanayake, S.D., Cho, S.J., Kim, K.B., Chung, K.Y., Yang, X.Q., and Nam, K.W. (2014). Structural changes and thermal stability of charged $LiNi_xMn_yCo_zO_2$ cathode materials studied by combined in situ time-resolved XRD and mass spectroscopy. ACS Appl. Mater. Interfaces *6*, 22594–22601.

11. Faenza, N.V., Lebens-Higgins, Z.W., Mukherjee, P., Sallis, S., Pereira, N., Badway, F., Halajko, A., Ceder, G., Cosandey, F., Piper, L.F.J., and Amatucci, G.G. (2017). Electrolyte-induced surface transformation and transition-metal dissolution of fully delithiated $LiNi_{0.8}Co_{0.15}Al_{0.05}O_2$. Langmuir *33*, 9333–9353.

12. Cho, Y., Eom, J., and Cho, J. (2010). High performance $LiCoO_2$ cathode materials at 60 degrees C for lithium secondary batteries prepared by the facile nanoscale dry-coating method. J. Electrochem. Soc. *157*, A617–A624.

13. Sharifi-Asl, S., Soto, F.A., Nie, A.M., Yuan, Y.F., Asayesh-Ardakani, H., Foroozan, T., Yurkiv, V., Song, B., Mashayek, F., Klie, R.F., et al. (2017). Facet-dependent thermal instability in $LiCoO_2$. Nano Lett. *17*, 2165–2171.

14. Gachot, G., Grugeon, S., Eshetu, G.G., Mathiron, D., Ribière, P., Armand, M., and Laruelle, S. (2012). Thermal behaviour of the lithiated-graphite/electrolyte interface through GC/MS analysis. Electrochim. Acta *83*, 402–409.

15. Mukai, K., Inoue, T., and Hasegawa, M. (2017). Rationalizing thermal reactions of C_6Li_x negative electrode with nonaqueous electrolyte. J. Power Sources *366*, 185–192.

16. Dai, J.H., Shi, C., Li, C., Shen, X., Peng, L.Q., Wu, D.Z., Sun, D.H., Zhang, P., and Zhao, J.B. (2016). A rational design of separator with substantially enhanced thermal features for lithium-ion batteries by the polydopamine-ceramic composite modification of polyolefin membranes. Energ. Environ. Sci. *9*, 3252–3261.

17. Zhu, Y.S., Wang, F.X., Liu, L.L., Xiao, S.Y., Chang, Z., and Wu, Y.P. (2013). Composite of a nonwoven fabric with poly(vinylidene fluoride) as a gel membrane of high safety for lithium ion battery. Energ. Environ. Sci. *6*, 618–624.

18. Croce, F., Focarete, M.L., Hassoun, J., Meschini, I., and Scrosati, B. (2011). A safe, high-rate and high-energy polymer lithium-ion battery based on gelled membranes prepared by electrospinning. Energ. Environ. Sci. *4*, 921–927.

19. Roth, E.P., Doughty, D.H., and Pile, D.L. (2007). Effects of separator breakdown on abuse response of 18650 Li-ion cells. J. Power Sources *174*, 579–583.

20. Choudhury, S., Azizi, M., Raguzin, I., Gobel, M., Michel, S., Simon, F., Willomitzer, A., Mechtcherine, V., Stamm, M., and Ionov, L. (2017). Effect of fibrous separators on the performance of lithium-sulfur batteries. Phys. Chem. Chem. Phys. *19*, 11239–11248.

21. Miao, Y.-E., Zhu, G.-N., Hou, H., Xia, Y.-Y., and Liu, T. (2013). Electrospun polyimide nanofiber-based nonwoven separators for lithium-ion batteries. J. Power Sources *226*, 82–86.

22. Inoue, T., and Mukai, K. (2017). Roles of positive or negative electrodes in the thermal runaway of lithium-ion batteries: accelerating rate calorimetry analyses with an all-inclusive microcell. Electrochem. Commun. *77*, 28–31.

23. Zhang, M.X., Liu, L.S., Stefanopoulou, A., Siegel, J., Lu, L.G., He, X.M., and Ouyang, M.G. (2017). Fusing phenomenon of lithium-ion battery internal short circuit. J. Electrochem. Soc. *64*, A2738–A2745.

24. Li, J., Cameron, A.R., Li, H.Y., Glazier, S., Xiong, D.J., Chatzidakis, M., Allen, J., Botton, G.A., and Dahn, J.R. (2017). Comparison of single crystal and polycrystalline $LiNi_{0.5}Mn_{0.3}Co_{0.2}O_2$ positive electrode materials for high voltage Li-ion cells. J. Electrochem. Soc. *164*, A1534–A1544.

25. Gaulupeau, B., Delobel, B., Cahen, S., Fontana, S., and Herold, C. (2017). Real-time mass spectroscopy analysis of Li-ion battery electrolyte degradation under abusive thermal conditions. J. Power Sources *342*, 808–815.

26. Feng, X., Ouyang, M., Liu, X., Lu, L., Xia, Y., and He, X. (2018). Thermal runaway mechanism of lithium ion battery for electric vehicles: a review. Energy Storage Mater. *10*, 246–267.

27. Spotnitz, R., and Franklin, J. (2003). Abuse behavior of high-power, lithium-ion cells. J. Power Sources *113*, 81–100.

28. Bodenes, L., Naturel, R., Martinez, H., Dedryvere, R., Menetrier, M., Croguennec, L., Peres, J.P., Tessier, C., and Fischer, F. (2013). Lithium secondary batteries working at very high temperature: capacity fade and understanding of aging mechanisms. J. Power Sources *236*, 265–275.

29. Ouyang, M., Zhang, M., Feng, X., Lu, L., Li, J., He, X., and Zheng, Y. (2015). Internal short circuit detection for battery pack using equivalent parameter and consistency method. J. Power Sources *294*, 272–283.

30. Finegan, D.P., Darcy, E., Keyser, M., Tjaden, B., Heenan, T.M.M., Jervis, R., Bailey, J.J., Malik, R., Vo, N.T., Magdysyuk, O.V., et al. (2017). Characterising thermal runaway within lithium-ion cells by inducing and monitoring internal short circuits. Energ. Environ. Sci. *10*, 1377–1388.

31. Hammami, A., Raymond, N., and Armand, M. (2003). Lithium-ion batteries: runaway risk of forming toxic compounds. Nature *424*, 635–636.

32. Campion, C.L., Li, W., and Lucht, B.L. (2005). Thermal decomposition of LiPF6-based electrolytes for lithium-ion batteries. J. Electrochem. Soc. *152*, A2327.

33. Xiong, D.J., Ellis, L.D., Petibon, R., Hynes, T., Liu, Q.Q., and Dahn, J.R. (2017). Studies of gas generation, gas consumption and impedance growth in Li-ion cells with carbonate or fluorinated electrolytes using the pouch bag method. J. Electrochem. Soc. *164*, A340–A347.

34. Forestier, C., Grugeon, S., Davoisne, C., Lecocq, A., Marlair, G., Armand, M., Sannier, L., and Laruelle, S. (2016). Graphite electrode thermal behavior and solid electrolyte

interphase investigations: role of state-of-the-art binders, carbonate additives and lithium bis(fluorosulfonyl)imide salt. J. Power Sources *330*, 186–194.

35. Michalak, B., Berkes, B.B., Sommer, H., Bergfeldt, T., Brezesinski, T., and Janek, J. (2016). Gas evolution in $LiNi_{0.5}Mn_{1.5}O_4$/graphite cells studied in operando by a combination of differential electrochemical mass spectrometry, neutron imaging, and pressure measurements. Anal. Chem. *88*, 2877–2883.

36. Nam, K.-W., Bak, S.-M., Hu, E., Yu, X., Zhou, Y., Wang, X., Wu, L., Zhu, Y., Chung, K.-Y., and Yang, X.-Q. (2013). Combining in situ synchrotron X-ray diffraction and absorption techniques with transmission electron microscopy to study the origin of thermal instability in overcharged cathode materials for lithium-ion batteries. Adv. Funct. Mater. *23*, 1047–1063.

37. Zheng, J.X., Liu, T.C., Hu, Z.X., Wei, Y., Song, X.H., Ren, Y., Wang, W.D., Rao, M.M., Lin, Y., Chen, Z.H., et al. (2016). Tuning of thermal stability in layered $Li(Ni_xMn_yCo_z)O_2$. J. Am. Chem. Soc. *138*, 13326–13334.

38. Lin, C.K., Piao, Y., Kan, Y.C., Bareno, J., Bloom, I., Ren, Y., Amine, K., and Chen, Z.H. (2014). Probing thermally induced decomposition of delithiated $Li_{1.2-X}Ni_{0.15}Mn_{0.55}Co_{0.1}O_2$ by in situ high-energy X-ray diffraction. ACS Appl. Mater. Interfaces *6*, 12692–12697.

39. Zhan, C., Wu, T.P., Lu, J., and Amine, K. (2018). Dissolution, migration, and deposition of transition metal ions in Li-ion batteries exemplified by Mn-based cathodes—a critical review. Energ. Environ. Sci. *11*, 243–257.

40. Zhan, C., Lu, J., Jeremy Kropf, A., Wu, T., Jansen, A.N., Sun, Y.K., Qiu, X., and Amine, K. (2013). Mn(II) deposition on anodes and its effects on capacity fade in spinel lithium manganate-carbon systems. Nat. Commun. *4*, 2437.

41. Li, W.T., and Lucht, B.L. (2006). Lithium-ion batteries: thermal reactions of electrolyte with the surface of metal oxide cathode particles. J. Electrochem. Soc. *153*, A1617–A1625.

42. Han, S., Xia, Y., Wei, Z., Qiu, B., Pan, L., Gu, Q., Liu, Z., and Guo, Z. (2015). A comparative study on the oxidation state of lattice oxygen among $Li_{1.14}Ni_{0.136}Co_{0.136}Mn_{0.544}O_2$, Li_2MnO_3, $LiNi_{0.5}Co_{0.2}Mn_{0.3}O_2$ and $LiCoO_2$ for the initial charge–discharge. J. Mater. Chem. A *3*, 11930–11939.

43. Zeng, X.Q., Xu, G.L., Li, Y., Luo, X.Y., Maglia, F., Bauer, C., Lux, S.F., Paschos, O., Kim, S.J., Lamp, P., et al. (2016). Kinetic study of parasitic reactions in lithium-ion batteries: a case study on $LiNi_{0.6}Mn_{0.2}Co_{0.2}O_2$. ACS Appl. Mater. Interfaces *8*, 3446–3451.

JOUL, Volume *2*

Supplemental Information

Thermal Runaway of Lithium-Ion Batteries without Internal Short Circuit

Xiang Liu, Dongsheng Ren, Hungjen Hsu, Xuning Feng, Gui-Liang Xu, Minghao Zhuang, Han Gao, Languang Lu, Xuebing Han, Zhengyu Chu, Jianqiu Li, Xiangming He, Khalil Amine, and Minggao Ouyang

Supplemental information

Table S1. Basic information on the automotive battery.

	Cathode	Anode
Active material	SC-NMC532	Artificial Graphite
Conductive material	Super P	Super P
Binder material	PVDF	CMC+SBR
Weight ratio of Active:Conductive:Binder	94:4:2	94:2:4
Specific Capacity	151 mAh/g	340 mAh/g
Electrolyte	1 M $LiPF_6$ in EC/PC/DEC (1:1:1)	

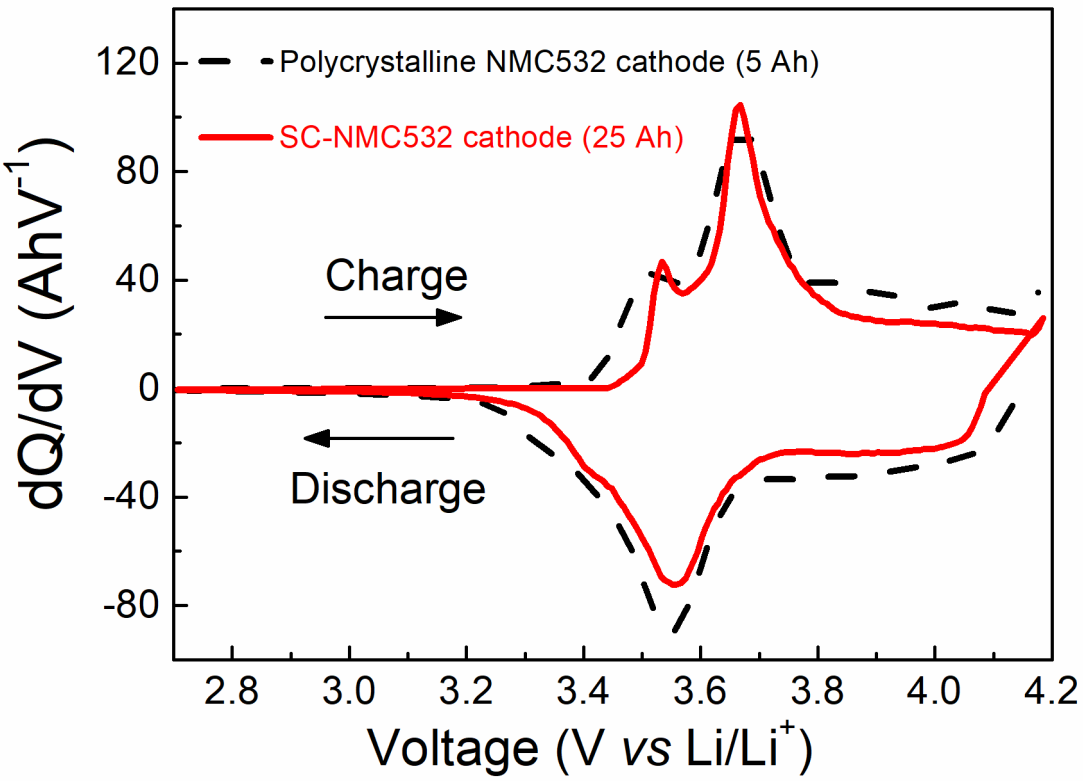

Figure S1. Comparison of the dQ/dV plots between the SC-NMC532/graphite battery with non-woven fabricated separator and ordinary pouch cell with NMC532 polycrystalline cathode. Note that the 5-Ah ordinary NMC532 cell also used a different separator, which is a PE/ceramic. Results show that the main charge and discharge redox peaks of SC-NMC532 are located at 3.56 V and 3.68 V, almost the same as for the polycrystalline cathode. However, their secondary redox peak during charge is different, which started at 3.43 V and 3.52 V for the polycrystalline and SC-NMC cathode, indicating the SC-NMC cathode is more stable than polycrystalline cathode.

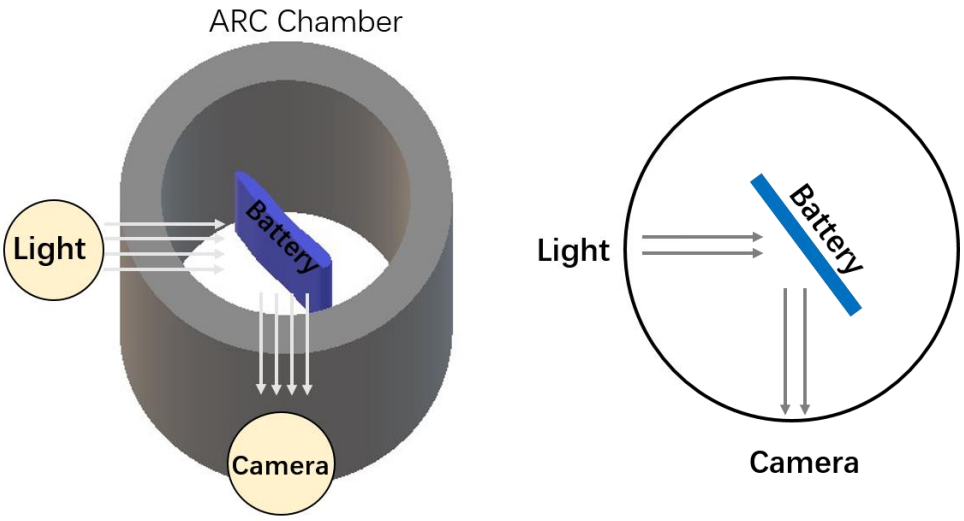

Figure S2. The video recording configuration of the ARC system.

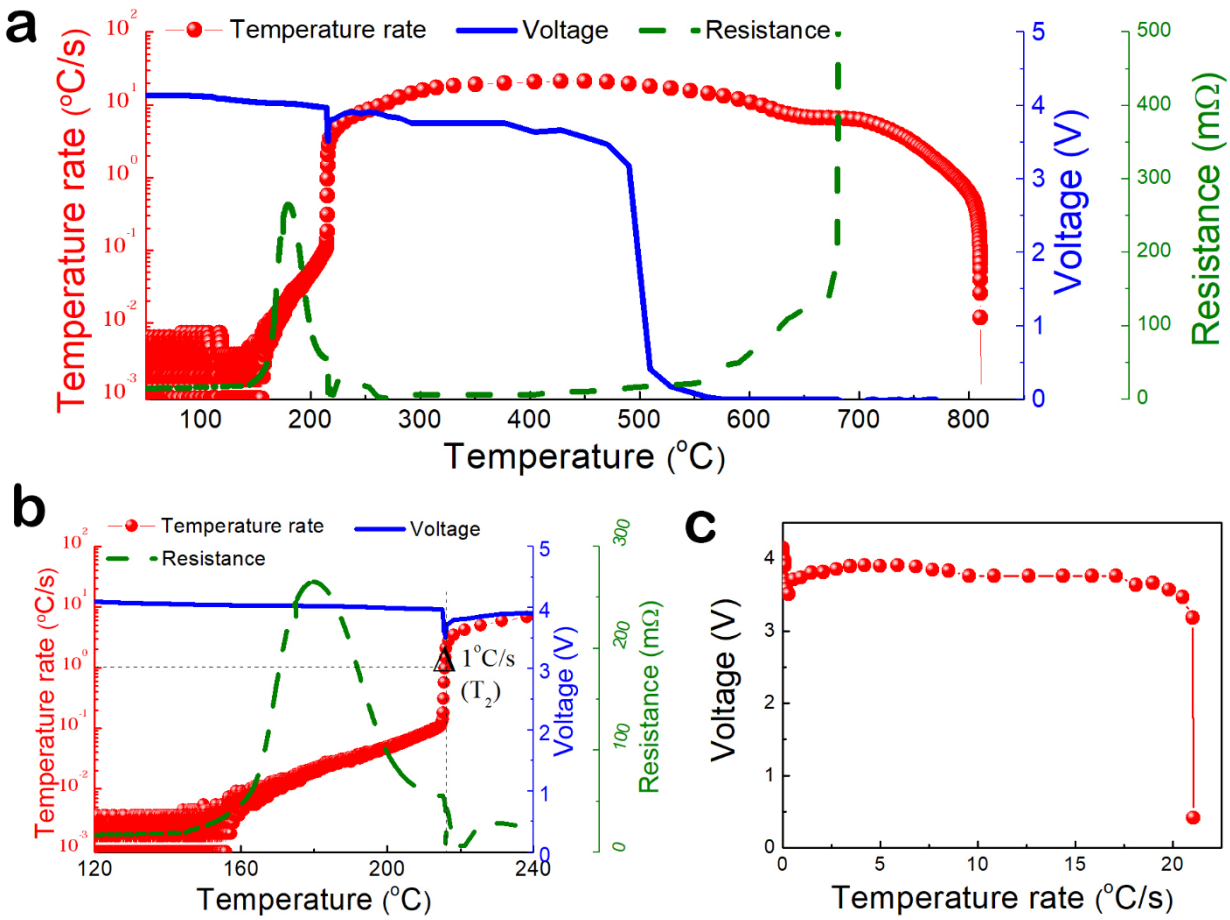

Figure S3. Thermal runaway characteristic plots of another SC-NCM532/graphite lithium-ion battery with a non-woven polyethylene terephthalate (PET)/ceramic separator. (a) Temperature rate, voltage, and resistance vs. temperature during thermal runaway measurement. (b) Segment of figure focused on thermal runaway onset temperature (T_2). (c) Relationship between the voltage and temperature rate during thermal runaway. The T_1, T_2, and T_3 for this battery are 115°C, 216°C, and 815°C respectively. The internal resistance increased from 15 mΩ at room temperature to 265 mΩ at 173°C, then dropped to 58 mΩ until T_2. The temperature increase rate reached a maximum of 21°C/s until the voltage dropped to zero.

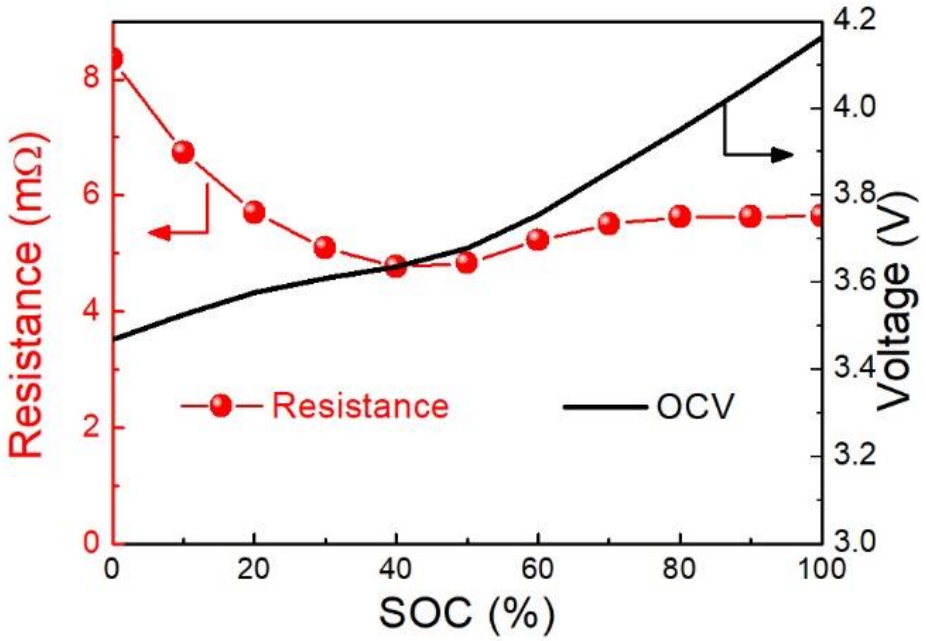

Figure S4. Battery internal resistance characterized by the hybrid pulse power characterization (HPPC) method, as well as the relationship between the state of charge (SOC) and open cell voltage (OCV).

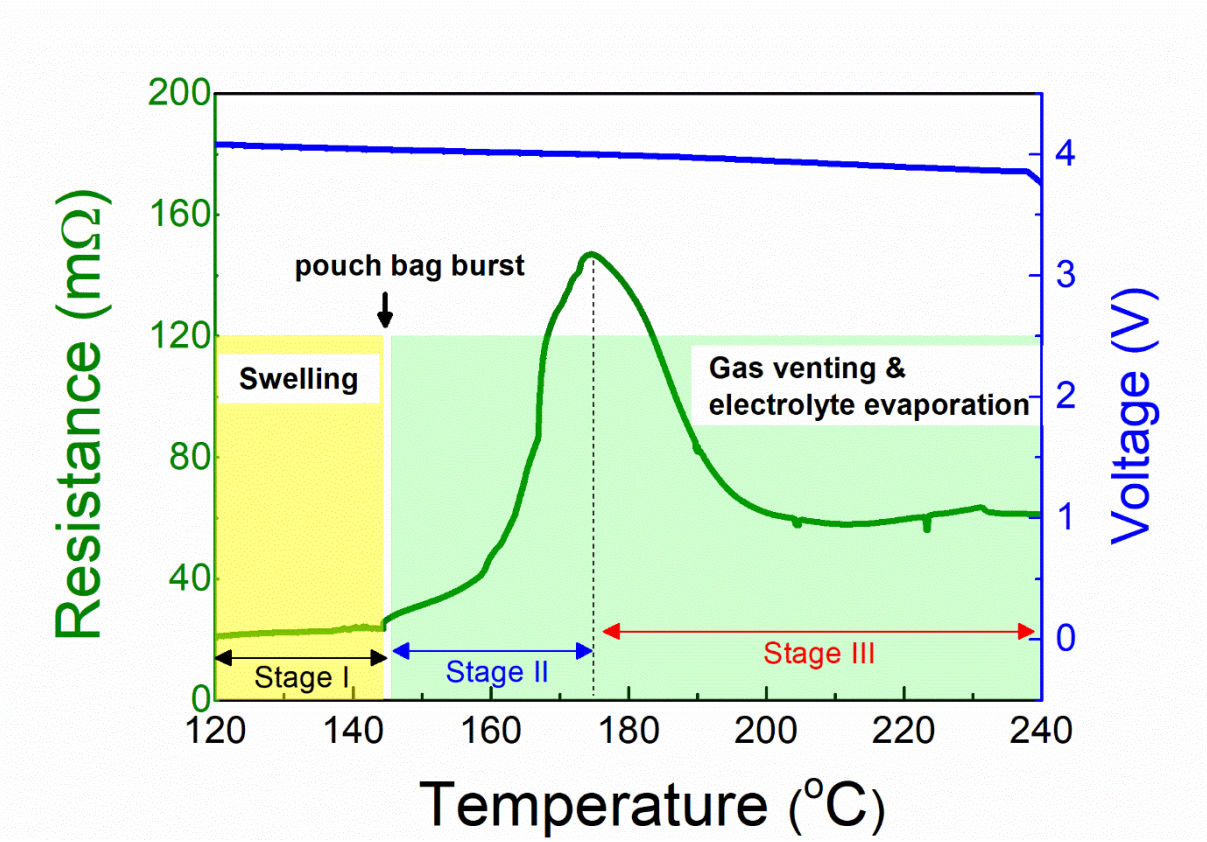

Figure S5. The swelling and venting temperature of the pouch bag battery according to the video, and the resistance curve before TR.

Table S2. The diameter, retention rate, and shrinkage of the separator with different temperatures.

	Pristine	230° C	250° C	270° C	290° C	330° C	350° C	400° C	450° C
Diameter (mm)	14.00	13.83	13.44	12.79	12.68	12.67	12.64	12.62	NA
Retention rate (%)	100	98.8	86.6	83.4	82.1	81.9	81.6	81.3	NA
Shrinkage (%)	0	1.2	13.4	16.6	17.9	18.1	18.4	18.7	NA

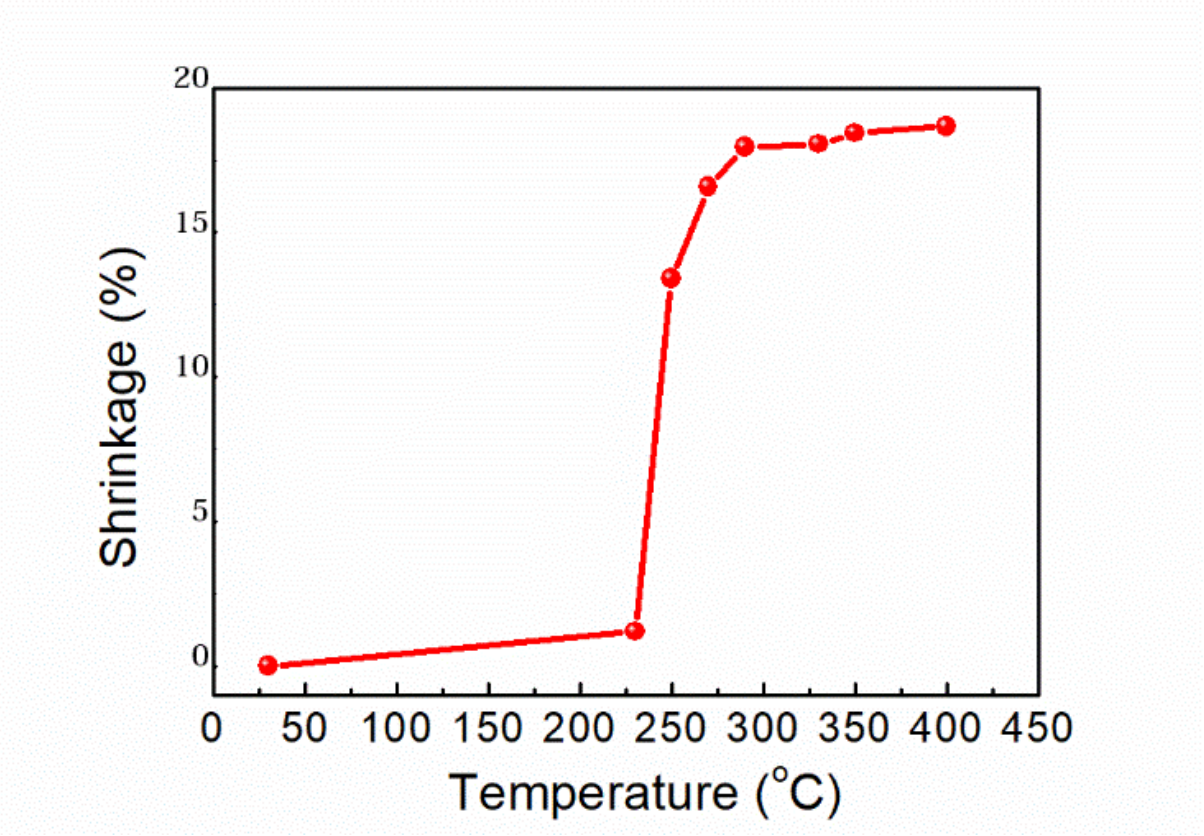

Figure S6. Shrinkage rate for the PET/ceramic separator with temperature.

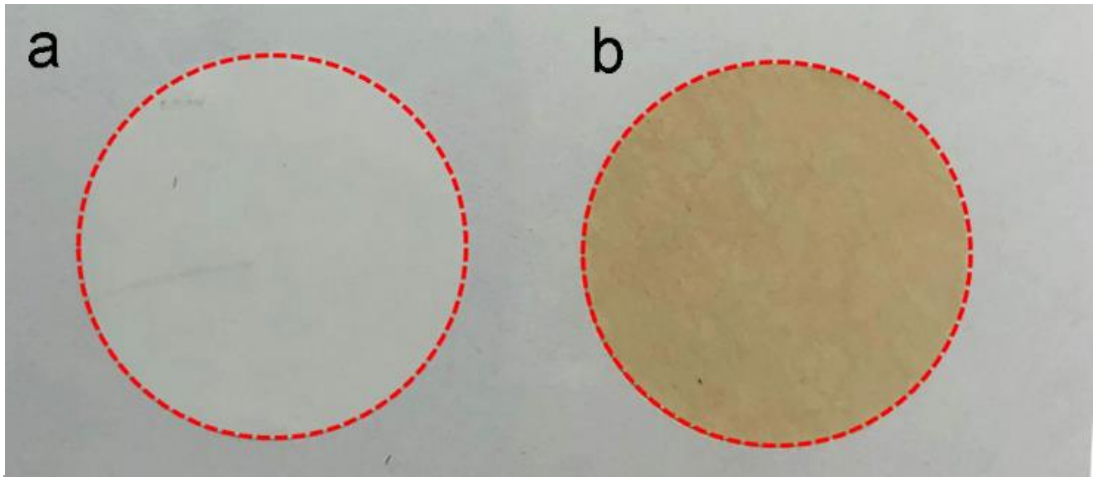

Figure S7. Comparison of the separator before and after hot box storage at 210°C for 13-hour. (a) Pristine separator (room temperature before the test). (b) Separator after 210°C hot box storage for 13 hours. Although the color changed to heavier grey compared to the pristine material, there is still no obvious shrinkage after the 13-hour 210°C storage. The result confirms that before the thermal runaway, there would be no serious internal short circuit caused by the separator shrinkage.

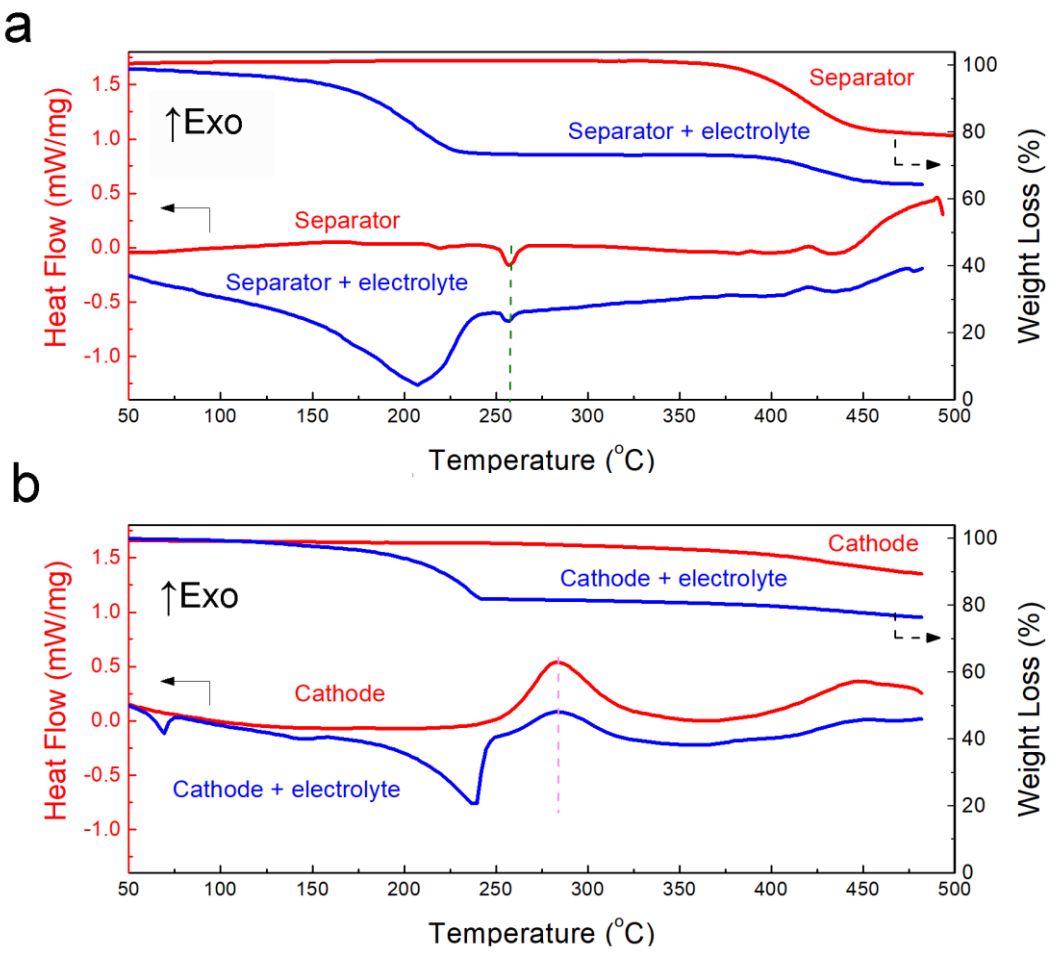

Figure S8. DSC and TG plots of (a) separator with and without electrolyte and (b) charged cathode with and without electrolyte.

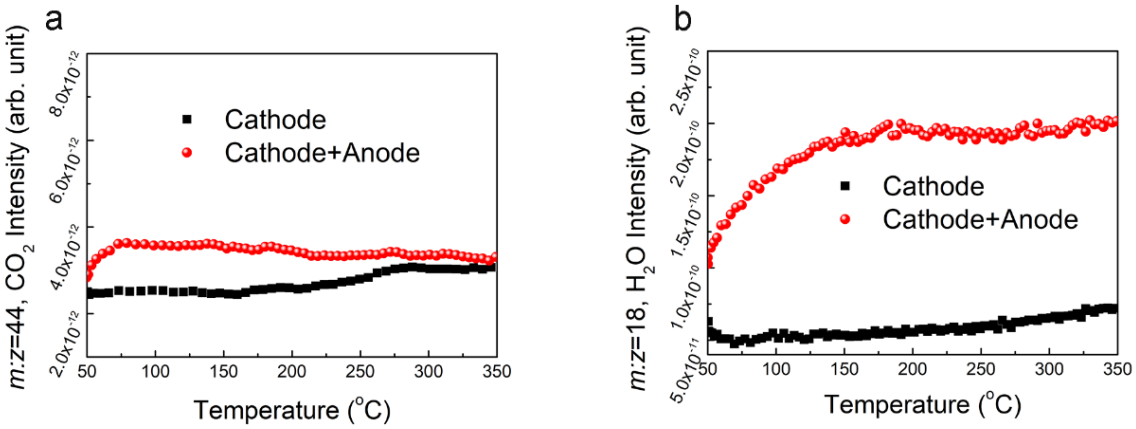

Figure S9. The mass spectroscopy result of mass-to-charge ratio of (a) 44 ($m:z$ = 44, CO_2) and (b)18 ($m:z$ = 18) for H_2O from the STA-MS measurement.

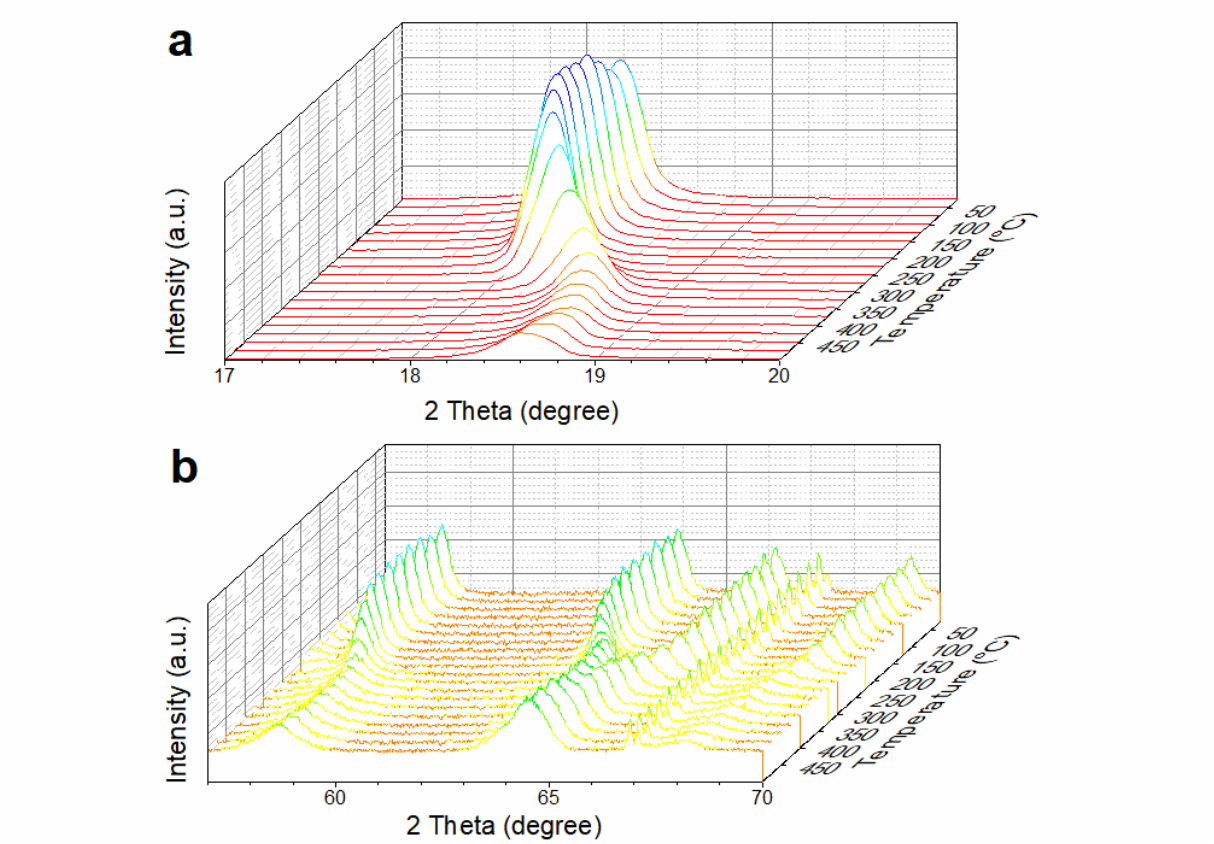

Figure S10. Temperature-resolved XRD plots of charged cathode materials with different temperature from 25 ℃ to 500 ℃.

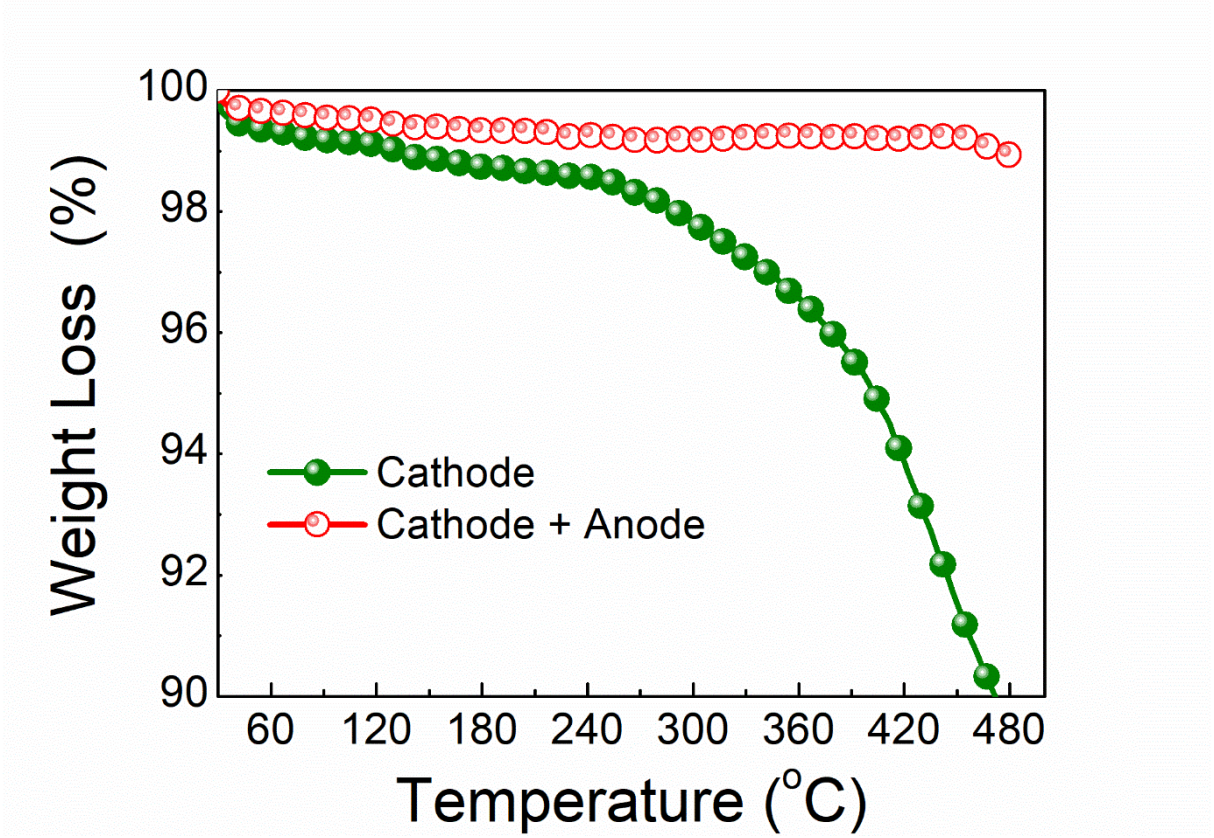

Figure S11. The chemical cross-talk between the charged cathode and anode. Weight loss comparison of charged cathode alone and cathode/anode mixture.

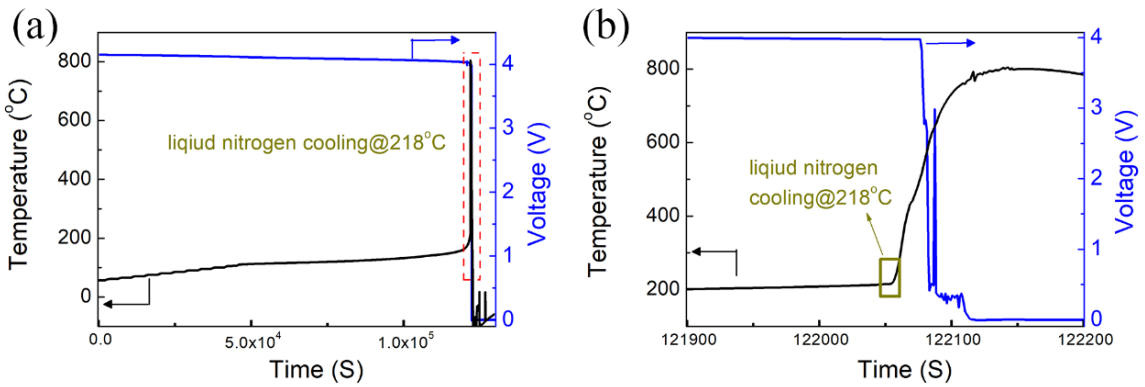

Figure S12. Even though liquid nitrogen purging at 218°C, the thermal runaway happened all the same. (a) Temperature and voltage curves of the ARC test during liquid nitrogen purging. The maximum temperature is 813°C, which is almost the same without the liquid nitrogen purge. (b) Segment of (a) for the thermal runaway process. The result indicates that the TR reaction is too severe to be prevented, even by liquid nitrogen.

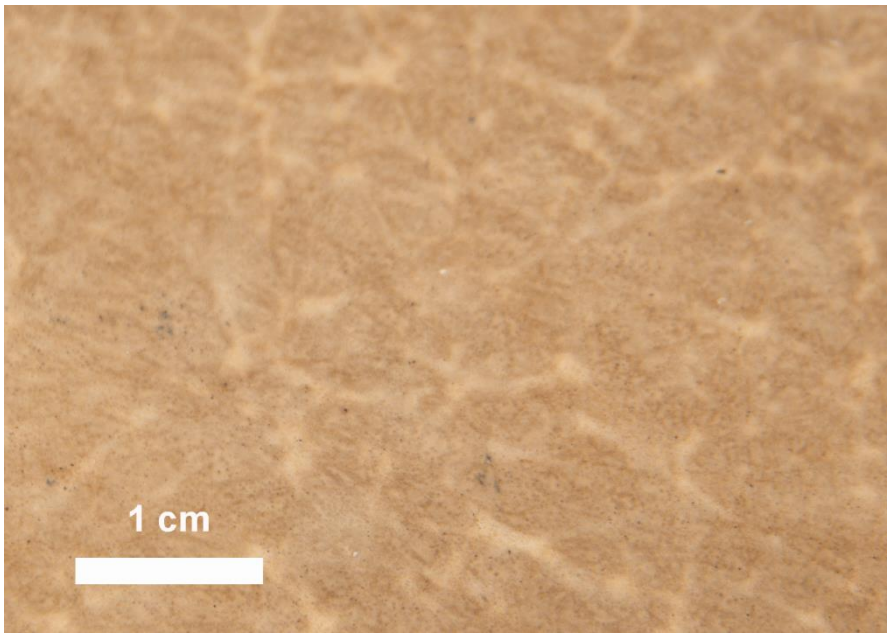

Figure S13. The optical image of the PET/ceramic separator before TR. The image shows the the integrity of the separator with no hole or damage.

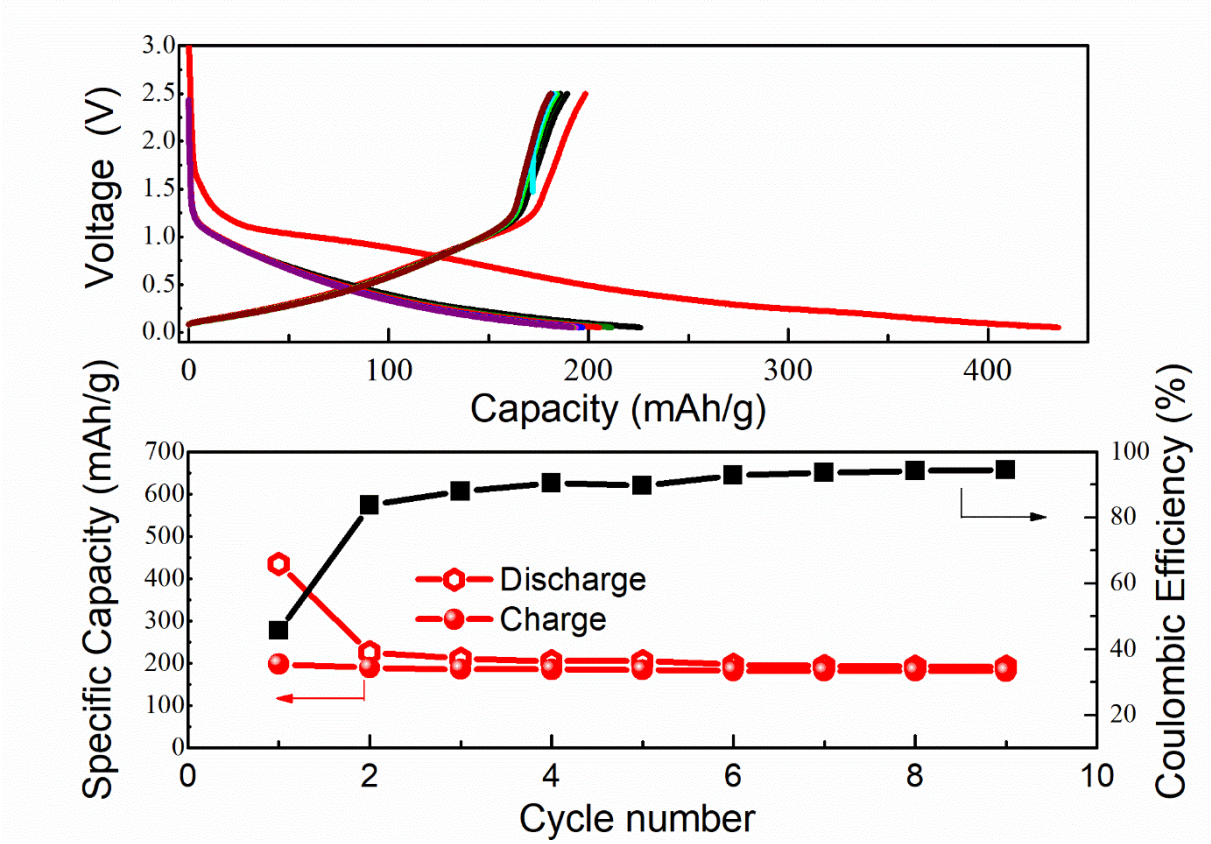

Figure S14. The cycling performance of the harvested separator after liquid nitrogen cooling of 206°C. The coin cell was assembled with a hard carbon anode and lithium foil counter electrode. The cycling performance confirmed that the harvested separator can still work functionally upon charge and discharge at 0.2C, proving that the self-heating is not driven by the internal short circuit but by the chemical crosstalk.

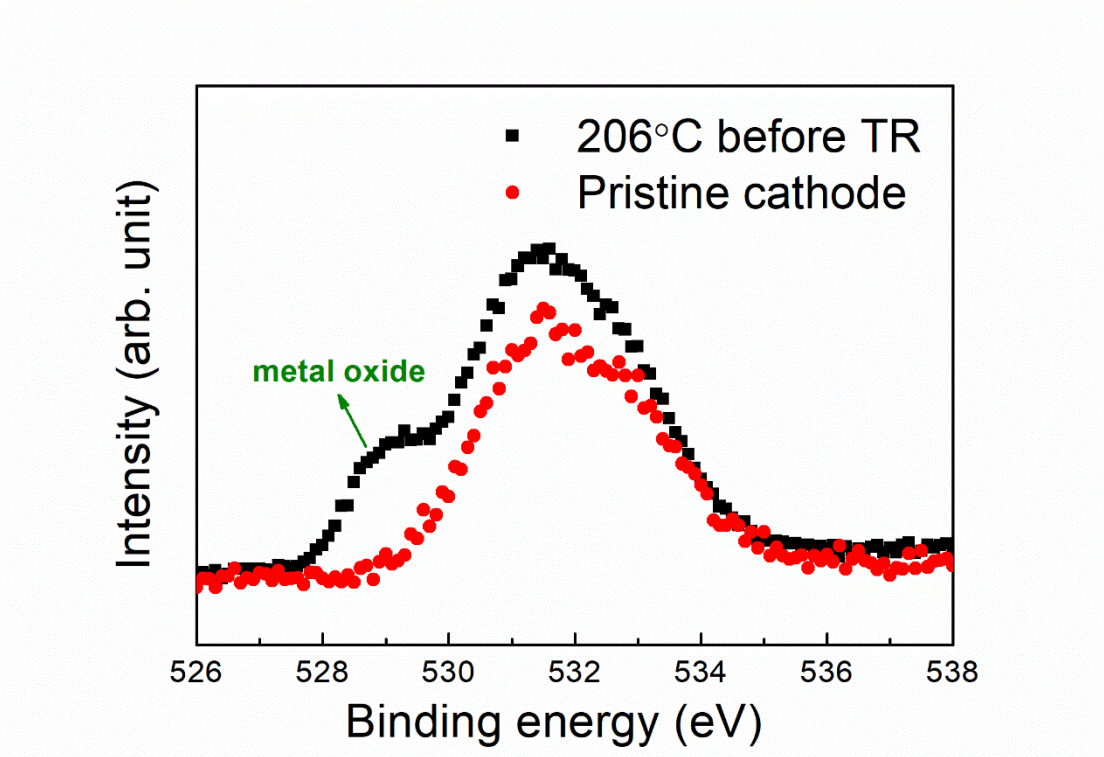

Figure S15. XPS analysis of pristine charged cathode and cathode with 206°C before thermal runaway. An additional peak regarding the metal oxide was detected on the sample before the thermal runaway.

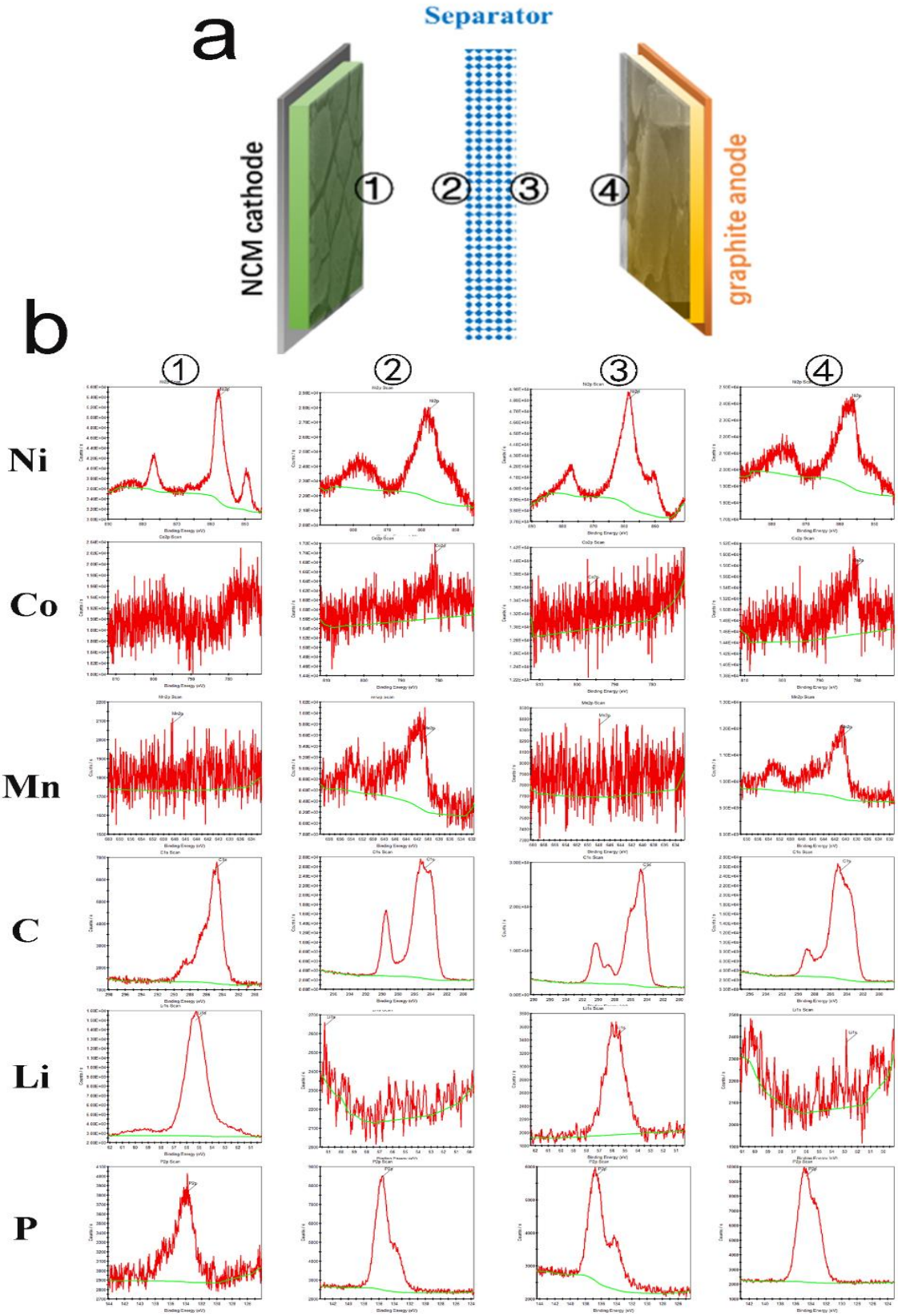

Figure S16. The XPS measurements of the automotive cell on different surfaces before TR. The Ni, Mn, and Co from cathode elements are detected on the separator and anode surface (fresh battery with one single charge), indicating the chemical crosstalk between the cathode and anode may not only trigger the TR by oxygen release, but also may occur during the self-heating process.